ARTICLE IN PRESS

Available online at www.sciencedirect.com

ScienceDirect

Advances in Space Research xxx (xxxx) xxx

ADVANCES IN SPACE RESEARCH (a COSPAR publication)

www.elsevier.com/locate/asr

Trajectory options for RAMSES' Farinella CubeSat around (99942) Apophis

Carmine Giordano *, Lucia F. Civati, Carmine Buonagura, Alban Beshaj, Iosto Fodde, Paolo Panicucci, Felice Piccolo, Elena Pilo, Pietro Califano, Fabio Ferrari, Francesco Topputo

Department of Aerospace Science and Technology, Politecnico di Milano, via La Masa, 34, Milan 20156, Italy

Received 12 March 2026; received in revised form 25 May 2026; accepted 20 June 2026

Abstract

The 2029 close approach of near-Earth asteroid (99942) Apophis presents an unprecedented opportunity to investigate tidal effects on a rubble-pile body and to advance planetary defense capabilities. In response, the Rapid Apophis Mission for SpacE Safety (RAMSES) has been conceived by the European Space Agency. In order to deliver additional science and complement the scientific objective, RAMSES includes two 6U-XL CubeSats, of which RAMSES CubeSat-1 (RCS-1), named Farinella, is dedicated to the characterization of Apophis's internal structure and surface properties via a low-frequency radar and high-resolution optical camera from an orbital perspective. This paper investigates the possible trajectory options for RCS-1, allowing the CubeSat to fulfill the scientific objectives, while respecting engineering constraints. To this aim, a high-fidelity dynamical model of Farinella proximity environment, incorporating a polyhedral gravity field, solar radiation pressure, and third-body perturbations from the Sun, Earth, and Moon, is implemented and analyzed. Three classes of candidate trajectories, namely patched hyperbolic arcs, Sun-stabilized terminator orbits, and resonant terminator orbits, are evaluated against scientific return and technical feasibility, considering the spacecraft specifications and instrument requirements that drive orbit design. A detailed trade-off, considering a 21-day timespan preceding the Earth close encounter, is then performed to select the baseline operational orbit, showing that both low-to-medium energy resonant orbits and medium-to–high altitude Sun-synchronous terminator orbits enjoy the best balance among all the considered criteria.

Keywords: Apophis; RAMSES; CubeSat mission; Planetary protection; Asteroid science

1. Introduction

Apollo-class asteroid (99942) Apophis, having a diameter of roughly 340 m, attracted considerable attention in December 2004 when early calculations suggested up to a 2.7% chance of an Earth impact on April 13, 2029 (Chesley, 2005). Follow-up tracking has since refined its trajectory and eliminated any collision risk (Giorgini et al., 2008), yet Apophis is still set to skim just 31000 km above Earth, that is well within the orbit of geostationary satellites (Sokolov et al., 2012). Although the prospect of an impact has been set aside, the flyby influence on Apophis itself remains an open question (Zhang and Michel, 2020), largely due to the limited knowledge about its internal structure. As the asteroid sweeps past, tidal forces from Earth's gravity will impart substantial torques, potentially altering

* Corresponding author.

E-mail addresses: carmine.giordano@polimi.it (C. Giordano), lucia-francesca.civati@polimi.it (L.F. Civati), carmine.buonagura@polimi.it (C. Buonagura), alban.beshaj@polimi.it (A. Beshaj), iosto.fodde@polimi.it (I. Fodde), paolo.panicucci@polimi.it (P. Panicucci), felice.piccolo@polimi.it (F. Piccolo), elena.pilo@polimi.it (E. Pilo), pietro.califano@polimi.it (P. Califano), fabio1.ferrari@polimi.it (F. Ferrari), francesco.topputo@polimi.it (F. Topputo).

https://doi.org/10.1016/j.asr.2026.06.067

0273-1177/

Please cite this article as: C. Giordano, L. F. Civati, C. Buonagura et al., Trajectory options for RAMSES' Farinella CubeSat around (99942) Apophis, Advances in Space Research, https://doi.org/10.1016/j.asr.2026.06.067

Apophis's shape, spin state, and surface characteristics (Souchay et al., 2014; Valvano et al., 2022). Depending on its material strength and cohesion, this close encounter might trigger anything from faint seismic ripples and minor regolith shifts (DeMartini et al., 2019; Scheeres et al., 2005; Ballouz et al., 2024), to widespread landsliding or even wholesale surface reconfiguration (Yu et al., 2014; Kim et al., 2023). That uncertainty makes the 2029 passage a rare chance for both planetary defense research and fundamental asteroid science. A dedicated spacecraft mission could not only document these tidal effects in real time but also shed light on Apophis interior structure, a knowledge that is essential for designing effective mitigation strategies against any future asteroid threat (Binzel et al., 2021).

As direct consequence of this celestial event, NASA has recently announced that Apophis will be the selected target of OSIRIS-REx extended mission (DellaGiustina et al., 2022), while ESA proposed RAMSES (Rapid Apophis Mission for SpacE Safety) mission, a fast-response initiative designed to rendezvous with Apophis prior to its Earth encounter (Kueppers et al., 2023; Morelli et al., 2024). Its objective is to accompany the asteroid during the fly-by in order to determine the physical and dynamical changes induced by the interaction with the gravity of the Earth. Among the mission payloads, two 6U-XL CubeSats will be included, one of which is RAMSES CubeSat-1 (RCS-1), named also Farinella, after the Italian planetary scientist Paolo Farinella[1]. RCS-1 will be deployed as part of RAMSES proximity operations and will orbit Apophis with the aim to complement the scientific objectives of the RAMSES spacecraft to enhance planetary defense demonstration efforts, to enable multi-point observations, and to facilitate closer and riskier operations. Specifically, Farinella aims to 1) characterize Apophis internal structure, and 2) characterize surface properties, through the use of a scientific optical camera and a low-frequency radar. The onboard optical camera has to capture high-resolution images of Apophis surface, allowing for detailed mapping of geological features, surface roughness, and dust distribution. Meanwhile, the low-frequency radar is designed to penetrate beneath the surface, providing critical data on internal layering, density variations, and structural characteristics. All this data will be used to assess asteroid characteristics pre- and post-encounter and to detect changes induced by the asteroid during its close approach with the Earth.

Due to strict timeline imposed by the close approach timeframe, with a launch at the latest in May 2028, RAMSES is intended to reuse and adapt the Hera spacecraft design as much as possible (Kueppers et al., 2023), and so are its CubeSats. Specifically, RCS-1 is expected to leverage the know-how and technologies acquired during the development of Hera's Milani.

[1] See https://www.esa.int/ESA_Multimedia/Images/2026/02/Ramses_CubeSat_Farinella_contract_signature. Last accessed on February 25, 2026.

Recent works have highlighted the importance of coupling shape-based gravity models, surface-environment analyses, and trajectory design when operating around irregular small bodies. In this context, the geophysical, surface, and orbital environments of asteroid 2016 HO3 have been investigated using irregular-shape dynamical models (Li and Scheeres, 2021; Li et al., 2023), while trajectory concepts around irregular asteroids have also been explored for applications such as ejecta-material collection from libration-point orbits (Burattini et al., 2024). These studies confirm that the irregular gravity field, surface geometry, and perturbation environment can strongly affect both the design and the assessment of proximity trajectories. Thus, the goal of the paper is twofold: to develop a high-fidelity model of the dynamical environment near Apophis and to investigate suitable trajectory options that can be exploited by RCS-1 during its scientific mission, with dedicated focus on the scientific phase preceding the Earth close encounter. This step is non-trivial for RAMSES because Apophis' 2029 close approach produces a strongly time-varying proximity environment, where the dominant third-body perturbation changes over the mission timeline and the relative weight of perturbations can vary by orders of magnitude over a few days. In addition, the CubeSat's high area-to-mass ratio makes solar radiation pressure competitive with gravitational terms already at modest distances, while the irregular, non-spherical gravity field is relevant in the tight operational altitude range. This work provides an analysis-driven methodology that explicitly copes with such a multi-regime environment, quantifying when simplified models break down, and using the resulting high-fidelity framework to screen and trade candidate trajectory families against science, guidance and navigation, and operational constraints, ultimately supporting a credible baseline orbit selection for Farinella.

The paper is organized as follows. In Section 2, the models for the CubeSat, the asteroid, and the dynamics are presented, considering all relevant perturbations and a high-fidelity representation of the asteroid gravity field. Then, Section 3 present an analysis on the dynamical environment. In Sections 4 and 5, a trade-off on the possible different approaches and the selection of a baseline trajectory is shown, respectively. Final remarks are given in Section 6.

2. CubeSat and environmental models

This section presents the assumptions and numerical models used in the preliminary assessment for the operational orbits of Farinella. After detailing the model of the CubeSat, information on the asteroid environment and dynamical models are provided.

2.1. CubeSat model

RCS-1 is a 6U-XL CubeSat, whose main characteristics are given in Table 1. These parameters are needed to define

Table 1
Relevant parameters of RCS-1.

Parameter	Symbol	Value
Mass	m	14.8 kg
Area	A	0.5329 m^2
Reflectivity coefficient	C_r	1.29

the dynamical model and to compute the solar radiation pressure (SRP) acting on the CubeSat.

RCS-1 will be equipped with a scientific optical camera and a low-frequency radar in order to fulfill its scientific objectives. Specifically, the camera will be exploited 1) to provide complementary observations to the RAMSES mission with the aim to characterize the effects of the close flyby of Apophis, and 2) to support the RAMSES radio-science experiment. On the other hand, the objective of the radar is twofold: 1) it must characterize Apophis internal structures, and 2) it must measure average Apophis permittivity. Additionally, the optical scientific camera is exploited to infer the spacecraft state by means of optical navigation. Characteristics of the camera and the radar are provided in Tables 2 and 3, respectively, while constraints and requirements related to science and navigation are listed in Table 4 and 5, respectively.

2.2. Asteroid model

Apophis is modeled as an irregular asteroid in a tumbling spin state. While its shape model and tumbling state have still significant uncertainties, a polyhedral shape model, adapted from (Brozović et al., 2018), is used both for dynamical and scientific purposes. Fig. 1 shows the polyhedral model as rendered in CORTO, (Pugliatti et al., 2023), modified by adding procedurally generated boulders MONET (Buonagura et al., 2024).

The full tumbling spin state of Apophis, as described in (Pravec et al., 2014), is computed and exploited to evaluate the scientific and navigation performances. Fig. 2 shows a schematics of Apophis rotational state. As per (Pravec et al., 2014), Apophis is in a low-amplitude non-principal-axis rotation state. These states are characterized by multiple periods. In case of Apophis, a two-period solution best approximate its light curve. Specifically, Apophis appears to be in a short-axis-mode, corresponding to rotation about its shortest axis at a period $P_{\bar{\phi}_l}$ and that axis wobbling around the angular momentum vector with an average period P_ψ. The vector of angular momentum $\mathbf{H}$, on the other hand, points toward a fixed direction. The angle between the rotation axis and the angular momentum θ changes quite significantly, since Apophis is nearly symmetric. The evolution of this angle in February 2029 is shown in Fig. 3.

All the other physical and inertial properties of Apophis are retrieved primarily from (Pravec et al., 2014; Valvano et al., 2022; Brozović et al., 2018). Differently from other sources, in this work the density of Apophis is not

Table 2
Key parameters for the camera.

Parameter	Value
Field of View (angular)	19.72 × 14.86 deg
Field of View (metric)	174 m @ 500 m distance
	695 m @ 2 km distance
Resolution	10 cm/px @ 589 m distance
	40 cm/px @ 2356 m distance

assumed, but computed as a derived parameter of the volume (given by the shape model) and the mass, in order to keep consistency among all the different parameters. The dynamical and orbital properties of Apophis, on the other hand, are retrieved from the up-to-date orbital kernel provided by the JPL Horizon system[2], retrieved on December 10, 2024. A summary of all the relevant parameters is provided in Table 6.

2.3. Dynamical model

A high-fidelity model of the dynamical environment in the proximity of Apophis has been implemented. All relevant gravitational and perturbing accelerations acting on the CubeSat are considered. In particular, the gravitational effect of the asteroid $\mathbf{a}_P$, which takes into account its non-spherical and irregular shape, is considered, together with the acceleration due to the SRP $\mathbf{a}_{SRP}$, and the perturbations due to Apophis heliocentric motion $\mathbf{a}_{3b}$, which include Sun, Earth, and Moon gravitational pulling, modeled as a third-body effect. The relative dynamics of Farinella near Apophis is investigated in a non-inertial reference frame, also referenced as ApophisFixed. This reference frame is centered at the Apophis barycenter. The z-axis is aligned with the asteroid's angular momentum, the x-axis toward Apophis prime meridian, and the y-axis to complete a right-handed triad.

In the most general form, the equations of motion for a point mass (i.e., the CubeSat) in the proximity of Apophis in the ApophisFixed frame read (Scheeres, 2012)

$$\dot{\mathbf{r}} = \mathbf{v} \tag{1a}$$

$$\dot{\mathbf{v}} = \mathbf{a}_A + \mathbf{a}_{SRP} + \mathbf{a}_{3b} - 2\boldsymbol{\omega} \times \mathbf{v} - \boldsymbol{\omega} \times (\boldsymbol{\omega} \times \mathbf{r}) - \dot{\boldsymbol{\omega}} \times \mathbf{r} \tag{1b}$$

with $\mathbf{r}$ and $\mathbf{v}$ the position and velocity, respectively, $\boldsymbol{\omega}$ the rotation vector of the ApophisFixed reference frame with respect to J2000, and $\dot{\boldsymbol{\omega}}$ its derivative.

To provide a suitable representation of the gravitational field in the close-proximity of the asteroid, a shape-based gravity model has been implemented. Exploiting the available polyhedral shape model, the acceleration field produced by Apophis is computed using the model by Werner and Scheeres (Werner, 1994; Werner and Scheeres, 1996), which considers the analytical gravitational potential of a constant-density polyhedral shape.

[2] See https://ssd.jpl.nasa.gov/horizons/. Last accessed on April 14, 2025.

Table 3
Key parameters for the radar.

Parameter	Value	Description
Antenna cone aperture	35 deg	The radar beam's angular width
Pulsing interval	10 s	Time between consecutive radar pulses
Number of sampling points	350,000	Number of points for complete coverage
Duty cycle	$\sim 27\%$	Ratio of active observation time to total time
Observation duration	45min	Active radar observation period per sequence
Inactivity period	2 h	Downtime between observation sequences

Table 4
Main scientific constraints & requirements.

	Constraints & Requirements
Optical Camera	• The shape of Apophis shall be measured with at least 40 cm resolution. • The surface topology of Apophis shall be measured with a coverage larger than 90% of the surface at 40 cm scale. • The camera shall image the surface at least 5 times with different phase angles between 0 and 90 degrees.
Low-Frequency Radar	• The spatial coverage during radar observations shall be maximized. • The CubeSat shall collect multiple measurement sequences per point on the surface of each asteroid target with varying acquisition geometries. Repetitiveness of ground tracks shall be avoided to favor variety of geometric configurations. • The radar observations shall be performed with distances from the surface between 1 and 3 km, with a maximum relative velocity of 1 m/s.

Table 5
Navigation constraints & requirements.

	Constraints & Requirements
Navigation	• Navigation process shall exploit optical measures to infer the estimated state. • For robustness' sake, trajectories where centroiding is possible (i.e., with distances larger than 1.4 km) shall be preferred. • Navigation algorithms are able to provide good performances when the asteroid is well illuminated (i.e., with a phase angle lower than 100 deg).

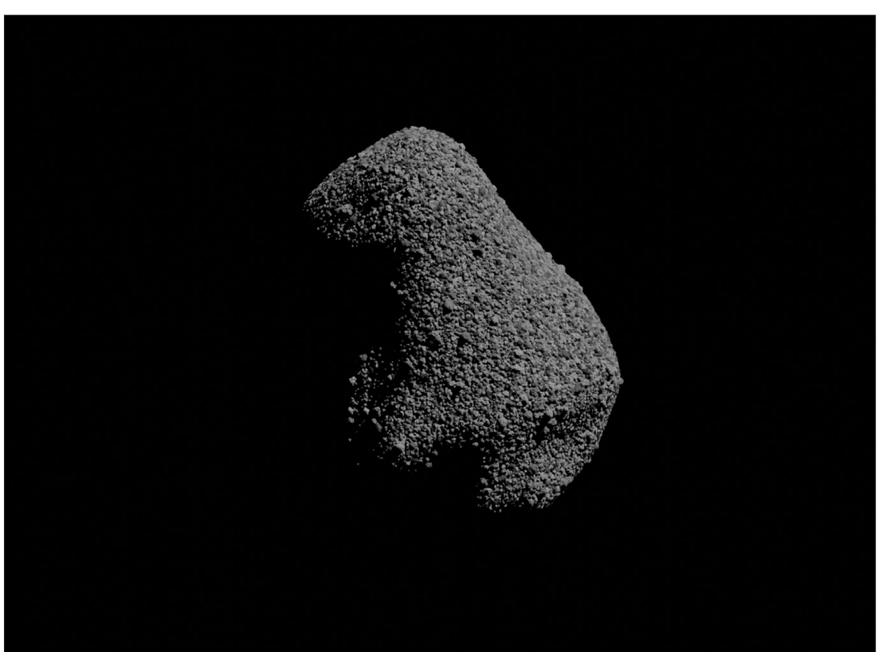

Fig. 1. Apophis polyhedral model as rendered in CORTO (Pugliatti et al., 2023).

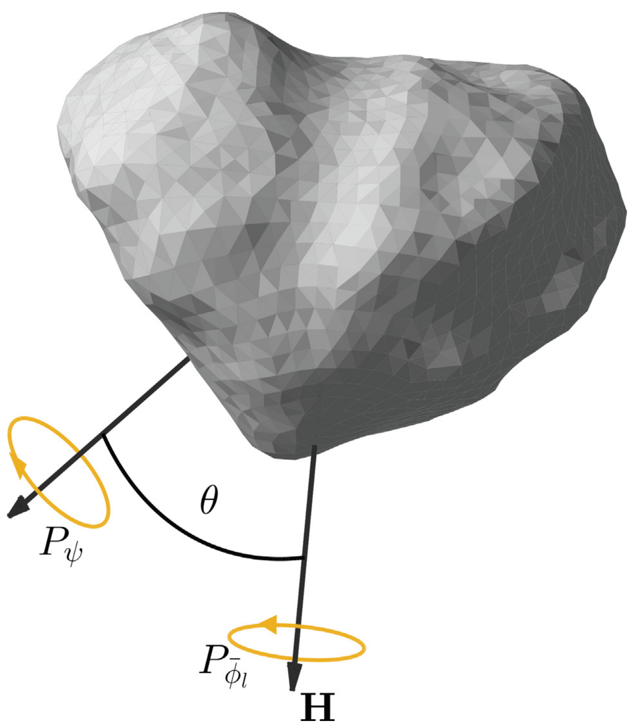

Fig. 2. Apophis rotational state in J2000 on April 13, 2029 (Pravec et al., 2014).

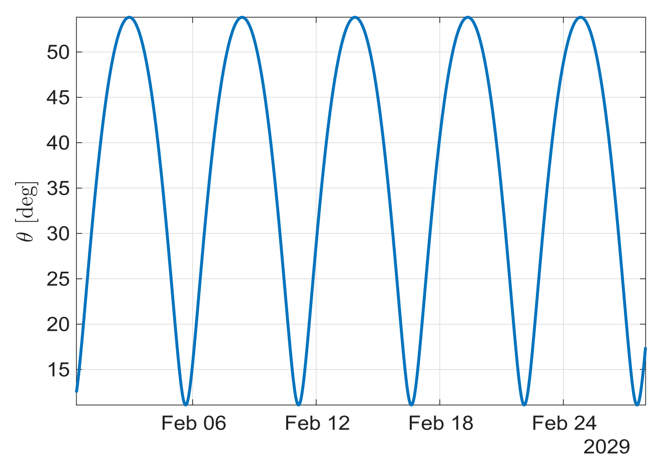

Fig. 3. Evolution of the tilt angle in February 2029 (Pravec et al., 2014).

Under this model, the Apophis gravitational acceleration can be computed as

$$\mathbf{a}_A = -G\rho\left(\sum_{e\in \mathrm{edges}} \mathbf{E}_e \cdot \mathbf{r}_e L_e - \sum_{f\in \mathrm{faces}} \mathbf{F}_f \cdot \mathbf{r}_f \kappa_f\right) \tag{2}$$

where G is the universal gravitational constant, ρ the density, $\mathbf{r}_e$ and $\mathbf{r}_f$ vectors from the field point to edge e and face f, respectively, and κ_f is the solid angle associated to face f, which for triangular faces is defined as

$$\kappa_f = 2\arctan\left(\frac{\mathbf{r}_i \cdot (\mathbf{r}_j \times \mathbf{r}_k)}{r_i r_j r_k + r_i(\mathbf{r}_j \cdot \mathbf{r}_k) + r_k(\mathbf{r}_j \cdot \mathbf{r}_i)}\right)$$

where, $\mathbf{r}_i, \mathbf{r}_j$, and $\mathbf{r}_k$, represent the vectors from the mesh geometric center to the vertices of face f. The dyad $\mathbf{E}_e$ associated to edge e can be computed as

$$\mathbf{E}_e = \hat{\mathbf{n}}_{f_1} \circ \hat{\mathbf{n}}_e^{f_1} + \hat{\mathbf{n}}_{f_2} \circ \hat{\mathbf{n}}_e^{f_2} \tag{3}$$

where $\hat{\mathbf{n}}_e^{f_1}$ and $\hat{\mathbf{n}}_e^{f_2}$ are the orthogonal to the faces sharing edge e, while $\hat{\mathbf{n}}_{f_1}$ and $\hat{\mathbf{n}}_{f_2}$ are the edge-normal vectors associated with edge e, while $\circ$ indicates the dyadic product. On the other hand, the dyad $\mathbf{F}_f$ associated to face f can be computed as

$$\mathbf{E}_e = \hat{\mathbf{n}}_f \circ \hat{\mathbf{n}}_f \tag{4}$$

where $\hat{\mathbf{n}}_f$ is the unit vector normal to face f. L_e is the potential of a wire associated to edge e, and it is

$$L_e = \ln\frac{r_i + r_j + e_{ij}}{r_i + r_j - e_{ij}} \tag{5}$$

with $e_{ij} = \|\mathbf{r}_j - \mathbf{r}_i\|$.

This model assumes a constant bulk density over the polyhedral shape. This is adequate for the preliminary trajectory-design trade-off performed in this work, but it neglects possible heterogeneities in the internal mass distribution of Apophis. Such heterogeneities may locally perturb the gravity field and affect the dynamical environment around irregular small bodies, as shown in (Wen and Zeng, 2023). The homogeneous polyhedral model is therefore used here as a nominal gravity model.

Table 6
Relevant parameters of Apophis.

Parameter	Symbol	Value	References
Total mass	M	4.5×10^{10} kg	(Brozović et al., 2018)
Ellipsoid semi-axes	(a, b, c)	(228.966, 159.026, 139.797) m	(Pravec et al., 2014)
Bulk density	ρ	2270kg/m^3	Derived from (Brozović et al., 2018)
Precession period	$P_{\bar{\phi}_l}$	27.38h	(Pravec et al., 2014)
Rotation period	P_ψ	263 h	(Pravec et al., 2014)
Sidereal main rotational period	P	30.56h	(Pravec et al., 2014)
Maximum axes ratio		0.965	(Pravec et al., 2014)
Minimum axes ratio		0.61	(Pravec et al., 2014)
RA and declination of **H**	(α_H, δ_H)	250, −75deg	(Pravec et al., 2014)
Pre-encounter semimajor axis	a^-	0.919AU	From JPL Horizon[2]
Post-encounter semimajor axis	a^+	1.101AU	From JPL Horizon[2]

The acceleration induced by the SRP on the CubeSat is computed by means of a cannonball model

$$\mathbf{a}_{SRP} = \frac{P_0}{c}\frac{D_{AU}^2 C_r A}{m}\frac{\mathbf{r}-\mathbf{r}_S}{\|\mathbf{r}-\mathbf{r}_S\|^3} \tag{6}$$

where P_0 (1367W/m^2) is the solar flux at 1AU, c is the speed of light (2.99792×10^5 km/s), D_{AU} is the Sun–Earth distance (with 1 AU equal to 1.496×10^8 km), C_r is the reflectivity coefficient of the CubeSat, A is its equivalent surface area, and m is its mass (as indicated in Table 1). The term $\mathbf{r}_S$ is the asteroid–Sun vector in the rotating frame. The SRP is considered only when the CubeSat is free of eclipses.

The third-body gravitational perturbations can be computed as

$$\mathbf{a}_{3b} = \sum_{i\in\mathscr{P}}(\mu_i+\mu_A)\frac{\mathbf{r}_i}{\|\mathbf{r}_i\|^3} - \mu_i\frac{\mathbf{r}-\mathbf{r}_i}{\|\mathbf{r}-\mathbf{r}_i\|^3} \tag{7}$$

where $\mathscr{P}$ is the collection of the perturbing bodies, namely the Sun, the Earth, and the Moon, μ_i their planetary gravitational parameter, $\mathbf{r}_i$ their position with respect to Apophis in the rotating frame, while $\mu_A = GM$ is Apophis gravitational parameter. The relative position between Apophis and the bodies is retrieved at each epoch from the ephemerides data. It can be noted, however, that $\mu_A \ll \mu_i$ for any perturbing body. Thus, Eq. (7) is simplified to

$$\mathbf{a}_{3b} = \sum_{i\in\mathscr{P}}\mu_i\left(\frac{\mathbf{r}_i}{\|\mathbf{r}_i\|^3} - \frac{\mathbf{r}-\mathbf{r}_i}{\|\mathbf{r}-\mathbf{r}_i\|^3}\right) \tag{8}$$

It is important to stress that all the three celestial bodies must be considered across the Earth close encounter as they are all relevant; see Section 3.

3. Dynamical environment

The dynamical environment close to Apophis is complex due to its irregular shape and the interaction with the different perturbating accelerations. Thus, their effects on the motion of a CubeSat should be assessed.

During Apophis close encounter (CE), the effects of the different accelerations acting on the CubeSat strongly change, mainly due to the proximity of Earth and Moon. Fig. 4 shows the accelerations acting on a field point as function of its distance from Apophis barycenter (left) and time (right). Acceleration ranges are shown during a three-days span, centered on the CE time on April 13, 2029, for a distance from Apophis barycentre ranging from 1 to 100 mean body radii. The shaded areas in the plots accounts for the variation of the acceleration over the considered timespan (on the left) and distance with respect to Apophis (on the right). In the near proximity of Apophis, the gravity of the asteroid (modeled, for simplicity, as central gravity) dominates over the other accelerations, but just after few body radii the dynamics are taken over by the Earth third-body effect, which becomes the most relevant effect at distances above 3 body radii. SRP and the Moon third-body effect overcome Apophis gravity above 15 and 40 body radii, respectively, while Sun third-body effect never dominates over the asteroid gravity in this time frame for distances below 100 body radii. Concerning time variation, Apophis gravity is time invariant, while the Sun gravity and SRP slightly increase due to the decrease in the Apophis–Sun distance. As anticipated, the strongest variation of dynamical environment in time is related to Earth and Moon's third-body perturbations; as shown in Fig. 4b, significant variations of these accelerations occur within a brief period during the CE. The Earth perturbation becomes dominant over the gravity of Apophis in the hours across the CE, while, in the two days after CE, the magnitude of Moon attraction becomes comparable to Apophis and Earth gravity. This behavior is unique with respect to past asteroid mission scenarios, in which the relative importance of the Sun third-body term changes slowly and the proximity environment can be approximated as nearly time invariant over the science phase. In the Apophis case, the CE forces a transition through distinct dynamical regimes, i.e., asteroid-dominated, Earth-dominated, and Earth–Moon comparable, over a short time window, making the selection of an adequate force model and the assessment of trajectory robustness highly sensitive to epoch. Therefore, the detailed analysis of Earth and Moon perturbations is not only descriptive, but a necessary step to define the validity domain of simplified models and to derive credible operational orbit options for Farinella.

The same analysis is repeated in Fig. 5 for the month before the close approach, in order to have a more comprehensive understanding of the environment during the whole Farinella mission. Also in this case, Apophis gravity is the dominant acceleration close to the body. However, after approximately 10 body radii the dynamics become governed by SRP.

Fig. 6 gives further insight into the relative importance of the different modeling assumptions during the month before the close approach. Differently from Figs. 4,5, Fig. 6 does not aim to represent the temporal variability of the perturbing accelerations. Instead, for each distance from Apophis, the maximum acceleration magnitude attained over the considered interval is retained, so as to provide a conservative comparison among the models. Four different models have been compared: 1) polyhedral model with all the perturbations, as explained in Section 2 (solid green line), 2) polyhedral model with SRP (dashed green), 3) only the gravity of Apophis with a polyhedral model (dotted green), and 4) only the gravity of Apophis with point-mass central field (red). This hierarchy allows the contribution of SRP and third-body perturbations to be separated from the error introduced by simplified gravity-field representations. The model considering all the effects and shape-based model is considered as the real-world reference, while other models are simplifications of the high-fidelity one. The comparison between

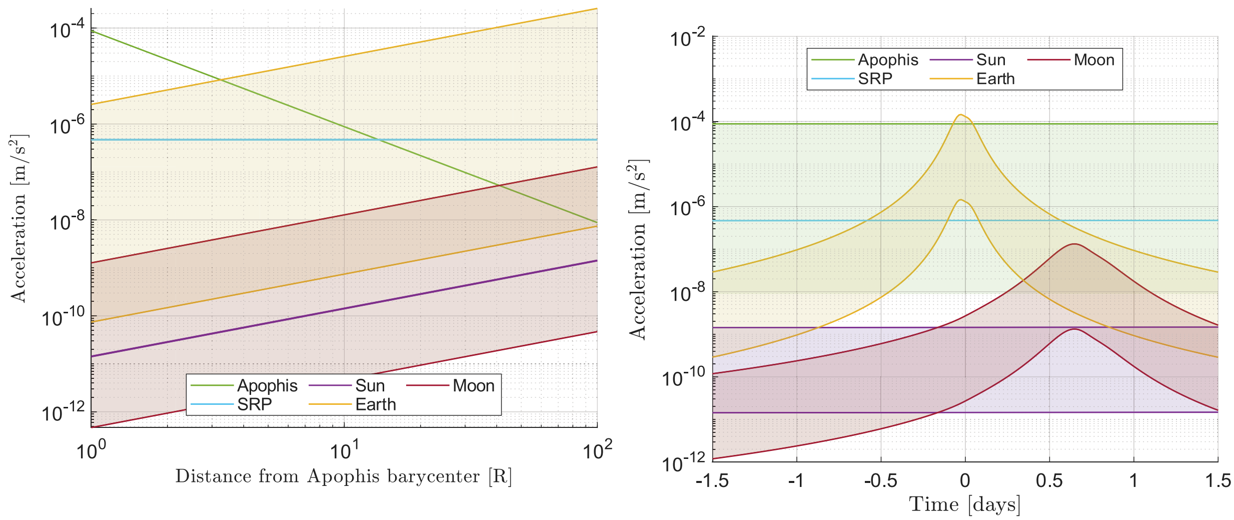

(a) (b)

Fig. 4. Main accelerations in the proximity of Apophis across the close approach. Gravity of Apophis, SRP, and three-body perturbations of Sun, Earth, and Moon, as function of (a) the distance from Apophis and (b) the relative time with respect the close approach are highlighted. Ranges between minimum and maximum values are shown as shadowed regions.

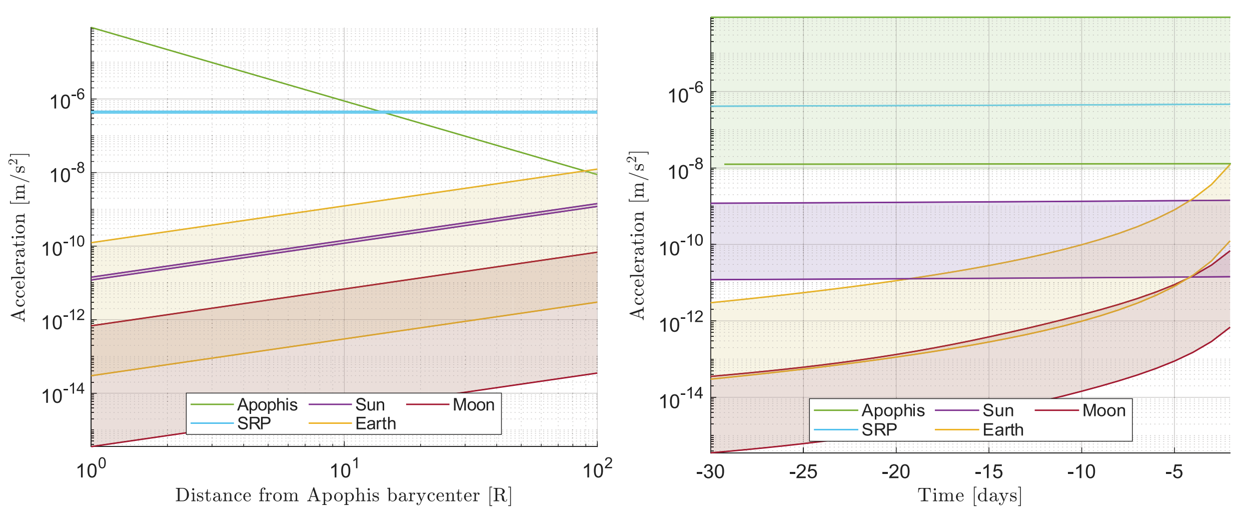

(a) (b)

Fig. 5. Main accelerations in the proximity of Apophis one month before the close encounter. Gravity of Apophis, SRP, and three-body perturbations of Sun, Earth, and Moon, as function of (a) the distance from Apophis and (b) the relative time with respect the close approach are highlighted. Ranges between minimum and maximum values are shown as shadowed regions.

high-fidelity and simplified models provides insightful information about the predominance of dynamical effects near Apophis. Left plot in Fig. 6 shows the acceleration field computed by each model, whereas the relative error (in percentage) between accelerations magnitudes computed in the simplified model versus the high-fidelity one is shown in the right plot.

It is clear that using the full high-fidelity model is needed to correctly represent the trajectory in close proximity. A simplified model for Apophis gravity could be used only relatively far from the asteroid. Indeed, in order to have a relative error less than 0.1% with the simplified model, the spacecraft must be further than 8 body radii (i.e., 1.5 km) from Apophis barycenter.

4. Operational trajectory design and trade-off

This section presents the design approach and methodology used to find a suitable operational orbit for Farinella in the vicinity of Apophis, able to accomplish the scientific and technological objectives of the mission.

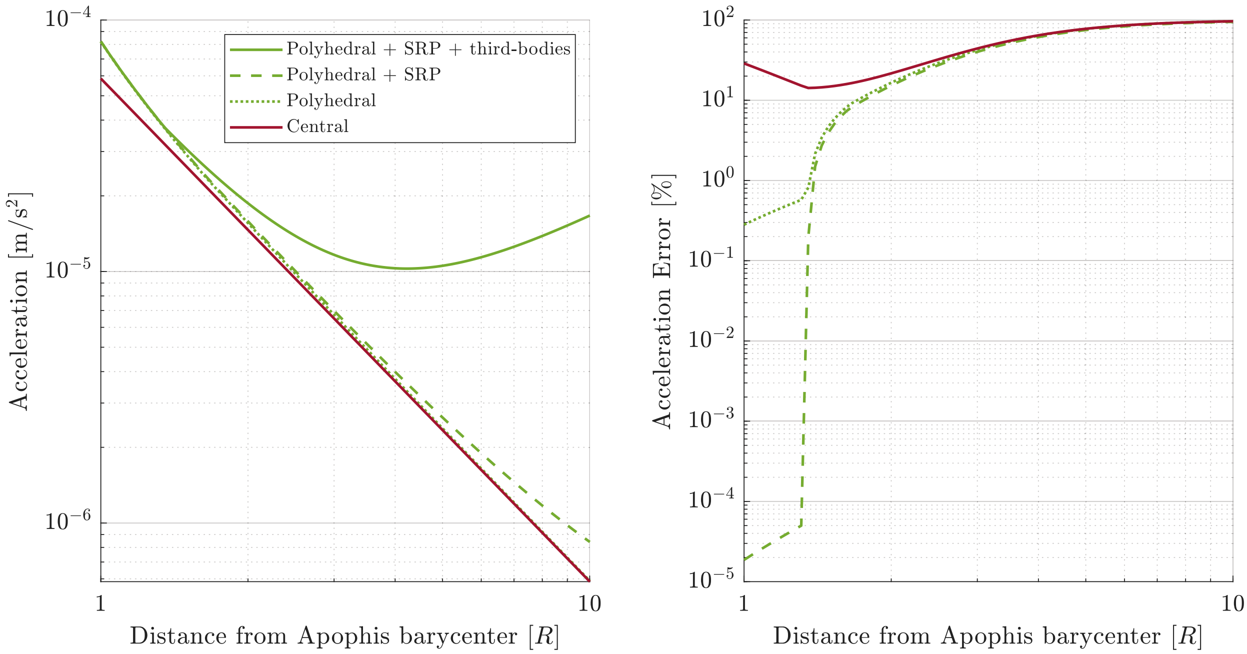

Fig. 6. Comparison between different acceleration models near Apophis during the pre-close-encounter scientific phase. For each distance from Apophis, the acceleration magnitude shown is the maximum value attained over the considered time interval. Absolute accelerations are shown in the left plot; relative errors with respect to the high-fidelity model are shown in the right plot. Third-bodies perturbations include the effect due to Earth, Moon, and Sun.

4.1. Constraints and drivers

The design space is characterized by several constraints, inferred by the payloads, the GNC system, and flight dynamics operations. Specifically, starting from Tables 4,5 and the heritage from Milani (Ferrari et al., 2021; Bottiglieri et al., 2023), the following constraints were formulated:

- **Scientific constraints**: RCS-1 must fly close to the asteroid to allow both high quality measurements by the radar and the camera. The radar requires also a non-null relative velocity with the asteroid surface to improve its scientific output, while the camera needs relatively low phase angles, to acquire images with the body illuminated. These constraints are not in contrast, but the radar and the camera require different possible trajectories for their optimal performances.
- **GNC constraints**: To enable visual-based navigation, trajectories with a low phase angle are preferred. Moreover, it is preferred to fly at distances where the central body is fully contained within the field of view of the camera, as this enables the use of centroiding algorithms for navigation, which are highly reliable. These constraints are similar, but not equal, to the ones associated with the scientific return of the camera.
- **Operational constraints**: RCS-1 can communicate with ground, sending data and receiving telecommands, only exploiting RAMSES as relay, that enjoys a 4–3-4–3-days repetitive pattern to contact the Earth. Flight dynamics operations require at least 48h to be completed. Open-loop maneuvers pose significant risks from the operational point of view and should be avoided. For these reasons, it is preferable to have a time between the maneuvers of at least 2 d and follow the same operational pattern given by RAMSES.The system poses additional attitude constraints to the flyable trajectories. For example, since the platform lacks a solar arrays driving mechanism, the spacecraft must assume a Sun-pointing attitude to generate power. Constraints on the attitude are given also by the scientific payloads (i.e., radar and camera must point toward Apophis). Trajectories that violate compatibility with these two pointing constraints must be discarded. Additional design drivers are also considered:

- **Safety**, in terms of risk to escape the asteroid or impact on it. The risk of impact on Apophis is assessed either a priori considering the safety factor C for open orbits, or by evaluating the orbit stability, in case of closed trajectories (Ferrari et al., 2021). Orbits too close to or too far from the asteroid, even if stable, are considered risky due to the probability of impact or escape, respectively. The highest priority is given to trajectories that are inherently safe, i.e., with $C > 0$ or with linear long-term stability. This consideration comes directly from the Milani mission design heritage (Ferrari et al., 2021).
- **Simplicity**, in terms of reduced operational burden to perform active operations on the CubeSat and optimization of the time allocated on RAMSES to relay CubeSat

operations. To accomplish this, the natural dynamics and perturbations of the asteroid environment can be leveraged to reduce the frequency of maneuvers. Compliance with this design driver is evaluated by considering the compatibility of the orbit with an operational pattern based on the 4–3-4–3-days pattern implemented by RAMSES.

- **Robustness** to the uncertainties due to the system and dynamical environment. This is tightly connected to safety and simplicity criteria. Inherently safe trajectories are typically more robust to uncertainties. On the other hand, long ballistic time of flights between consecutive maneuvers require robust trajectories, able to deal with uncertainties without jeopardizing the safety of the RAMSES mission or altering the mission profile strategy.
- **Cost**, in terms of Δv. Apophis dynamical environment is “slower” than the Didymos system, mainly due to the smaller gravitational parameter. Thus, smaller maneuvers than Milani ones are expected. Since RCS-1 will have the same propulsion system of Milani, costs are deemed not critical. For this reason, safe, simple, and robust trajectories are preferred, at a cost of higher Δv.

Given the constraints and drivers, a trade-off analysis is performed to select the scientific operational orbit. The performance of each option is assessed in terms of ability to meet the scientific constraints and compliance with the mentioned criteria in order to get at the end to a summarizing trade-off matrix.

4.2. Candidate orbits

The analysis of the dynamical environment in the proximity of Apophis (Section 3) highlighted the impossibility of orbiting the asteroid on a stable and purely Keplerian solution. This is due to the action of the SRP on the CubeSat and the pulling forces exerted by both the Earth and the Moon during the close approach. The CubeSat has a high area-to-mass ratio and, therefore, it is extremely sensitive to the dynamical effect of the SRP. For this reason, alternative solutions were sought. Farinella can fly on several orbit types, namely.

1) **Hyperbolic arcs**. Farinella might use hyperbolic (or parabolic) arcs. These orbits can grant bounded Sun phases angles, which is desirable for navigation purposes, and can involve safely hyperbolic arcs (beyond certain energies). Yet, they require a frequent trajectory control. This strategy has flight heritage in small-body environment. It was performed by Rosetta during its initial scientific phase after rendezvous with comet 67-P/Churyumov-Gerasimenko (Pérez-Ayúcar et al., 2018), and it is the strategy envisaged for Milani during its operational phases (Ferrari et al., 2021). The key aspect of a patched-arc strategy is the proper selection of waypoints (the manoeuvring points between ballistic arcs) (Ferrari et al., 2021). After selecting the waypoints, the trajectory is designed using a numerical targeter, by setting the duration of the arc to either 3 or 4 days, to be aligned with the operational pattern expected by RAMSES. The targeter finds a dynamically-compliant arc that connects two consecutive waypoints in a given flight time (Ferrari et al., 2021). This strategy is flexible in terms of waypoint selection, which can be set to meet observational and operational requirements. These trajectories are also designed to be always in the Sun-side region.In the Farinella case, the time spent inside the science admissible region should be maximized. Ideally, waypoints inside the admissible region could be selected, but they would be too close to each other and not compatible with a 3- or 4-day ballistic trajectory. A dedicated analysis of patched hyperbolic arcs for the Farinella operational scenario showed that even loops exiting from the admissible region would require a maneuver frequency higher than that allowed by the expected operational pattern (Azzola, 2024). Therefore, hyperbolic arcs are safe and enjoy good characteristics in terms of illumination and required attitude, but they are incompatible with operational constraints and ground resolution. Fig. 7a shows a case with a 2–2-3 manoeuvring pattern.
2) **Terminator orbits**. Farinella can leverage terminator-like orbits, which exploit the solar radiation pressure to stay in a bounded region with respect to the asteroid. Terminator orbits are well-known solutions to fly in close proximity to minor bodies. A particular type of orbit, called Sun-stabilized terminator orbits (SSTO) (Takahashi and Scheeres, 2020), have been used by OSIRIS-Rex during the close proximity operations about Bennu (McMahon et al., 2018) and they are planned for Juventas (Goldberg et al., 2019) as well as for the experimental phase of Milani. SSTO lie within a plane orthogonal to the Sun direction, slightly displaced in the anti-Sun direction. For this reason, they are free of eclipses, but they are characterized by phase angles higher than 90 deg. Additionally, their range from the main body is bounded and depends only on the characteristics of the asteroid and the CubeSat. In the case of Farinella, SSTOs have a maximum altitude of approximately 1.8 km. Low ranges and high phase angle pose a challenge for the optical navigation and optical measurements. On the other hand, this range can enable scientific operations with the radar. However, the relative velocity with the asteroid surface appears low; in the best case (i.e., at the equator) the relative speed is given by the spin of Apophis, and could be not enough to provide good scientific data. Fig. 7b shows an example of the SSTO with a range of 1.4 km.Starting from the SSTO, other terminator orbits can be

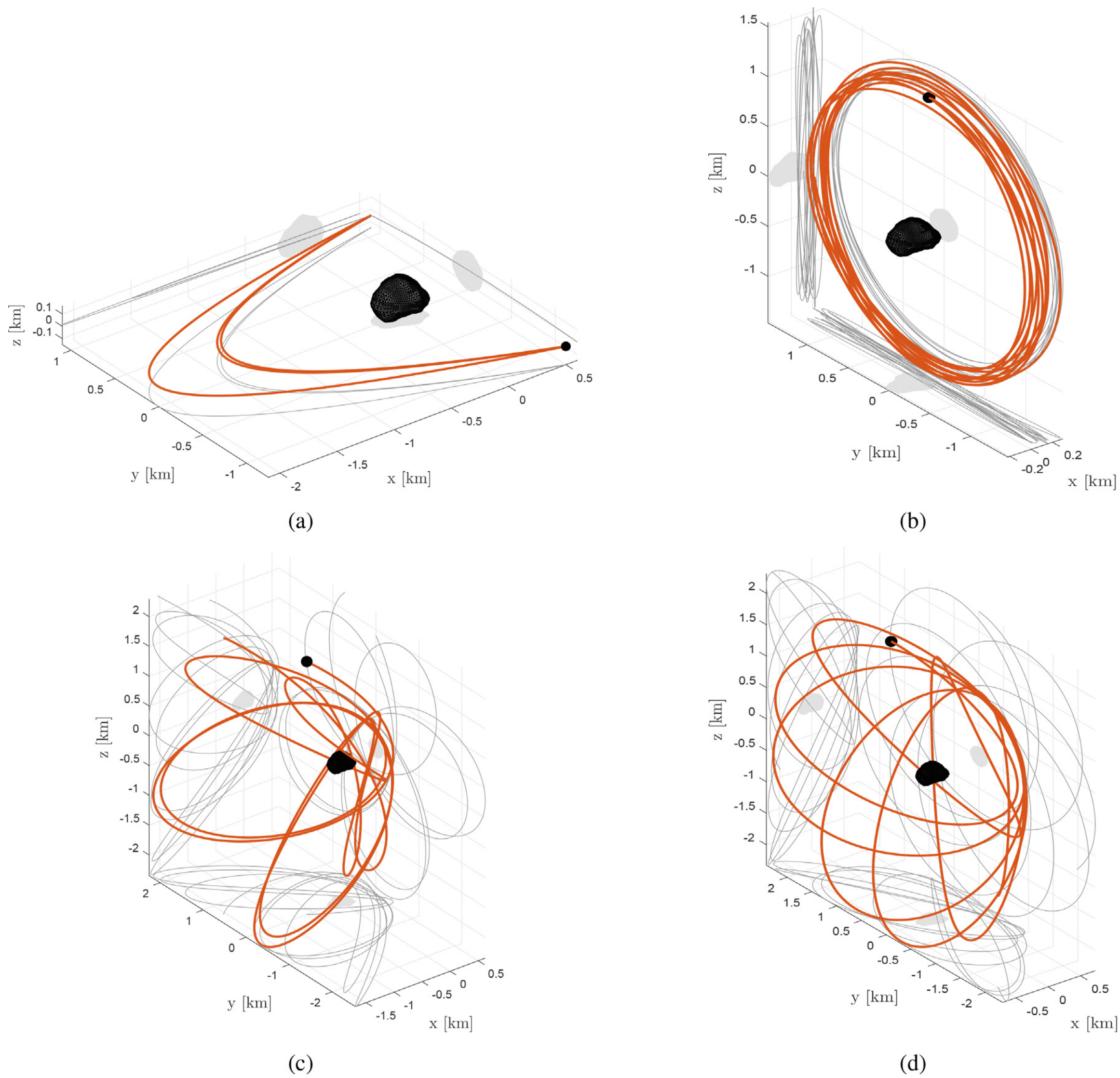

Fig. 7. Example of different candidate orbits: (a) 2–2-3-days hyperbolic arcs; (b) SSTO with a semimajor axis of 1.4 km; (c)-(d) RTO with different resonance and energy. Orbits are in the ApophisAntiSun reference frame, with the Sun direction corresponding to the negative x-axis (Broschart et al., 2014).

found by exploiting some dynamical characteristics. The most promising ones are the so-called resonant terminator orbits (RTO) (Broschart et al., 2014). They are called resonant, since they bifurcate from SSTO resonance. These trajectories are made of stable closed flower-like orbits, formed by repetitive precessing ellipses. Each ellipse has its apocentre in the Sun side (they have a long arc with good phase angles) and their pericenter in the night side (experiencing, so, short eclipses). A greater variety of RTOs can be found since it is possible to select both the resonance number and the energy. A higher resonance number means a slower trajectory (i.e., it has a larger period), while increasing the energy moves the RTO away from the SSTO, meaning that high energy RTOs have a more distant apocenter toward the Sun side. The combination of distances and phase angles, as well as the high relative velocity at the pericentre, could be beneficial for the scientific observations. Figs. 7d show two examples of RTOs.

3) **Hovering**. Farinella might hover, i.e., keep the position fixed in a given reference frame of interest, ensuring flexibility in the design and compliance with the observational requirements. In the case of Farinella, two different hovering strategies can be implemented: one is to keep the CubeSat fixed with respect to the Sun, or to hover along the Earth-Apophis line. In the first case, the phase angle can be selected arbitrarily and it is fixed, while in the second case it depends uniquely on the trajectory of Apophis. Unfortunately, in the latter case, the phase angle is in certain portions of the mission lifespan well above 90 deg, hindering both the camera and the navigation processes. On the other hand, hovering at a constant

phase angle poses problems for the radar, since the relative motion of the asteroid will be guaranteed only by its own rotation, which could be not enough to get good scientific data. It is important to highlight, however, that for both solutions an active control strategy is needed to keep the CubeSat in the desired location. In conclusion, while hovering is a simple solution to design and it is considered safe, it is expensive to implement, and it does not guarantee good characteristics from the scientific point of view.

4.3. Trade-off summary

We summarize all strategies considered to support science operations in the trade-off matrix reported in Table 7. The different orbit options described above have been traded against the identified most important criteria.

RTOs and SSTOs exhibit the best balance among all the criteria, and they could be used to perform different scientific measurements during the mission lifespan. Hyperbolic arcs, even if stable and with good characteristics for navigation, can be critical from the operational point of view, and hence they can be used only when a tight schedule can be guaranteed and safety is paramount (e.g., during the flyby). Hovering, similarly, is not an option for the operative orbit of RCS-1, but can be used during close approach to reduce the risk of escape and impact.

5. Baseline Operational Trajectory Analysis and Trade-Off

As per Table 5, the best balance among the different criteria is awarded to both the SSTO and RTO. However, these orbits exist in families and thus several orbits can be generated by varying one parameter, e.g., the semimajor axis (SSTO) or the energy at give resonance (RTO). In order to properly select the baseline operational orbit among the different possibilities, a detailed trade-off is performed on a subset of these orbits.

5.1. Trajectory options

The subset of operational orbits in the detailed trade-off is selected in order to encompass as much as possible the trade space of both SSTO and RTO. Specifically, the following options are considered.

- SSTO with semimajor axis between 0.8 and 1.8 km spaced by 0.2 km, that is 6 SSTO in total. The minimum (0.8 km) and maximum (1.8 km) ranges have been selected to assure safety against impact and escape, respectively.
- RTO with 3:1 and 4:1 resonance with 3 energy level each (-13, −11, −9), that is, 6 RTO in total. The two resonances (3:1) and (4:1) are selected since they are the lowest and highest unit resonances generating stable orbits. The boundary values for Jacobi energy are selected considering safety against impact and escape, respectively.

All the candidate trajectories are shown in Fig. 8. SSTOs are generated by following the methodology in (Takahashi and Scheeres, 2020), while RTOs are computed first in a simplified model in the ApophisAntiSun reference frame as per (Broschart et al., 2014), then propagated in the high-fidelity model. To distinguish among the different options, the following naming convention is adopted in the remainder of this paper:

Table 7
Science orbit trade-off matrix.

		Hyperbolic arcs	SSTO	RTO	Hovering (Sun)	Hovering (Earth)
Science with radar	Time	< 50%	100%	~ 100%	Depends on the distance	Depends on the distance
	Relative velocity	Good	Low	Discrete	Low	Low
Science with camera	Phase angle Distance	<90 deg Can vary	>90 deg Fixed	(60, 120) deg Can vary	≈0 deg Fixed	>90 deg Fixed
Operations	Time between maneuvers	<3 d	Only SK needed	Only SK needed	<2 d	<2 d
Navigation	Phase angle Distance	<90 deg >2 km	>90 deg <2 km	(60, 120) deg (0.5, 2.5) km	≈0 deg (1, 5) km	>90 deg (1, 5) km
Safety	Against escape or impact	Inherently safe trajectories	Safe trajectories	Safe trajectories	Escape is likely	Escape is likely
Simplicity	Compliant with 4-3-4-3 pattern	Partly 4-day arcs to be split	Yes	Yes	No	No
Robustness	Against uncertainties	Robust far from the body	Robust	Robust	Robust	Robust
Monthly Cost		≈1.5 m/s	<1 m/s	<1 m/s	>2.5 m/s	>2.5 m/s

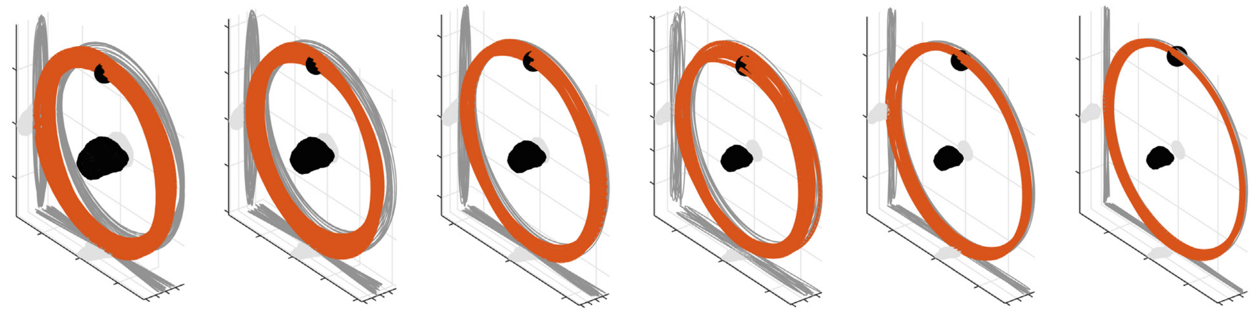

(a) Ensemble of the SSTO trajectory options, from semimajor axis equal to 0.8 km on the left, to 1.8 km on the right, with a 0.2 km step.

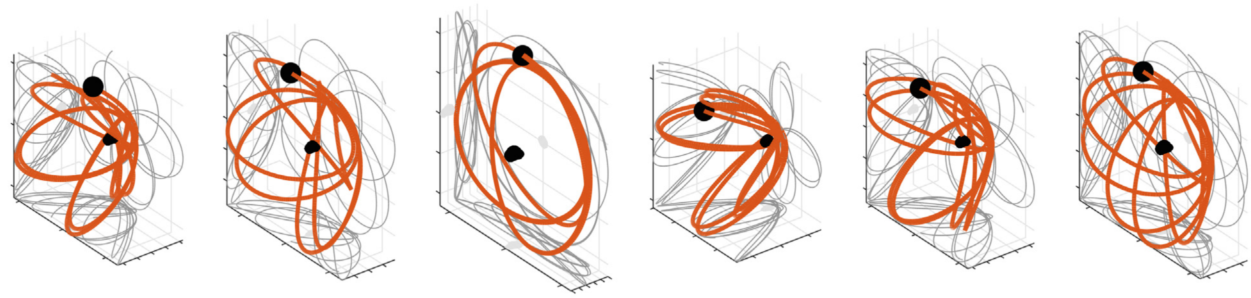

(b) Ensemble of the RTO trajectory options, from Jacobi constant equal to -9.0 on the left, to -13.0 on the right, with a 2.0 step. First three plots shows 4:1 resonant orbits, while last three plots shows 3:1 resonant orbits.

Fig. 8. Ensemble of all the 12 trajectory options.

- SSTO_apb indicates a SSTO with a nominal semimajor axis of a.b km (i.e., SSTO_1p2 is the SSTO with a semimajor axis of 1.2 km);
- RTO_mtn_Japb indicates a RTO of resonance m:n, with a nominal Jacobi energy of -a.b (i.e., RTO_3t1_J11p0 is the 3:1 RTO with J=-11.0).

5.2. Trade-off criteria

The 12 candidate options have been traded off against a number of criteria. For each criterion a performance index is defined to use in the detailed trade off matrix. For all the preliminary analyses, a timespan of 21 days representing the scientific phase before the CE is considered.

Scientific return Trajectory options must be primarily evaluated on the scientific return they can provide. For this reason, initial evaluations of the scientific output have been carried out.

A preliminary operation analysis for the radar is performed, considering characteristics and requirements as per Tables 3 and 4. For this preliminary radar analysis, a low-fidelity model of Apophis, represented as a sphere, is used. The radar analysis is intended only as a preliminary feasibility screening. The spherical approximation is used to assess whether the candidate trajectories provide global angular coverage and non-repetitive ground-track distributions, rather than to derive a final radar performance estimate. Therefore, local effects associated with the irregular shape of Apophis, tumbling attitude, detailed range, and relative-velocity constraints, and instrument-specific radar performance are not captured at this stage. The resulting coverage estimates should consequently be interpreted as first-order indicators. A dedicated high-fidelity radar assessment based on the polyhedral shape model and detailed observation geometry is foreseen in the following mission-design phases. The angular sampling criterion (Haynes et al., 2021) is used to determine and generate the number of sampling points on the sphere necessary to perform monostatic radar observations, ensuring a complete spatial coverage. The observed sampling points are evaluated at each radar sounding, with a pulse transmitted every 10 s. This evaluation considers the proposed observation sequence, an antenna cone aperture of 35 deg, and assumes that the radar is continuously pointing toward the center of the asteroid. The analysis shows that candidates orbits are fully capable to satisfy the radar coverage needs. More specifically, all proposed options ensure 100% coverage. Examples of the outcome of this analysis are shown in Figs. 9 and 10. For each trajectory, two visualizations are presented: on the left, a 2D coverage map of the asteroid surface, where each sampling point is color-coded based on the number of times it is observed; on the right, a ground-track plot of the trajectory on the asteroid surface, with the ground track during inactivity periods highlighted in blue and the ground track during activity periods shown in orange. These ground-track plots confirm that the proposed trajectories avoid repetitive patterns, which is beneficial for ensuring a diverse range of geometric configurations for observations. The time needed for each

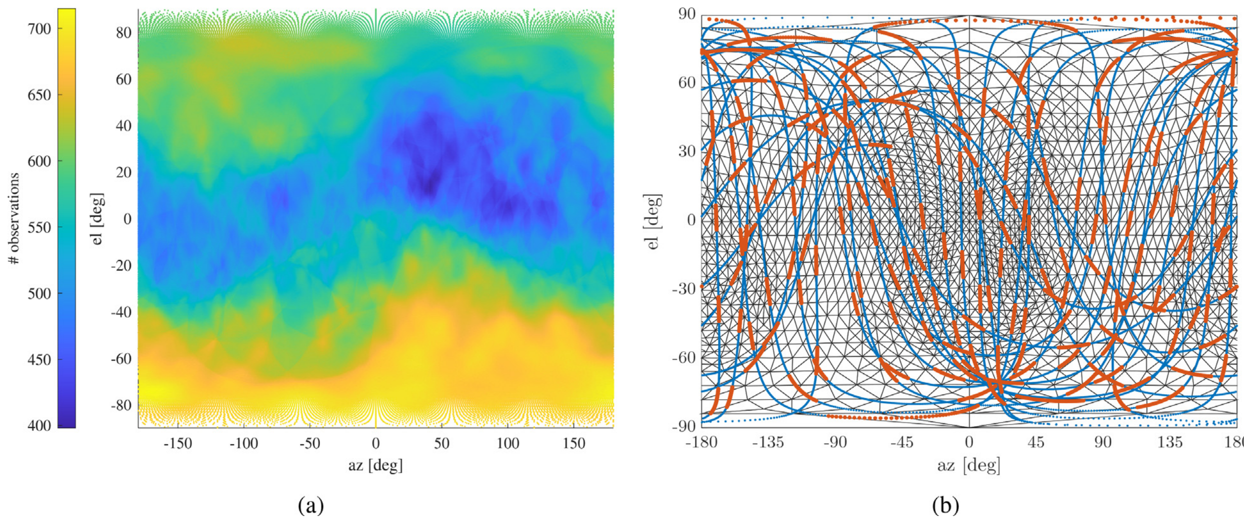

Fig. 9. Radar coverage analysis for SSTO_0p8: (a) 2D coverage map of the asteroid surface showing the number of radar observations per sampling point; (b) Ground-track of the CubeSat trajectory, with blue indicating inactivity periods and orange indicating activity periods.

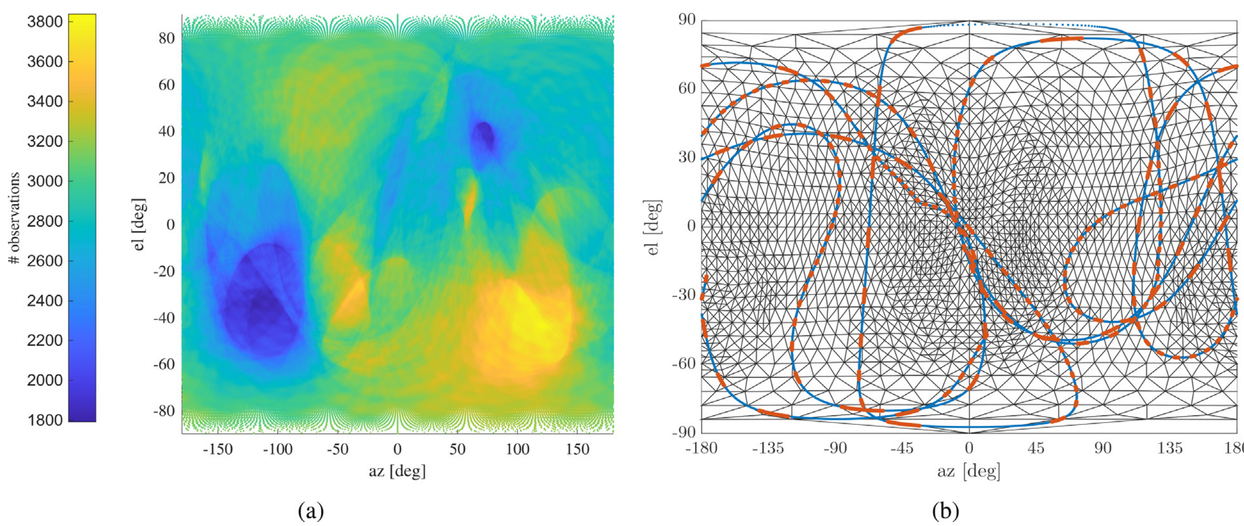

Fig. 10. Radar coverage analysis for RTO_4t1_J13p0: (a) 2D coverage map of the asteroid surface showing the number of radar observations per sampling point; (b) Ground-track of the CubeSat trajectory, with blue indicating inactivity periods and orange indicating activity periods.

Table 8
Time to reach complete coverage of the radar.

Type	ID	Time [h] ([d])
SSTO	SSTO_0p8	88.0 (3.66)
	SSTO_1p0	88.0 (3.66)
	SSTO_1p2	110.0 (4.58)
	SSTO_1p4	134.8 (5.61)
	SSTO_1p6	107.3 (4.47)
	SSTO_1p8	123.8 (5.16)
RTO	RTO_3t1_J9p0	189.8 (7.91)
	RTO_3t1_J11p0	242.0 (10.08)
	RTO_3t1_J13p0	170.5 (7.10)
	RTO_4t1_J9p0	203.7 (8.49)
	RTO_4t1_J11p0	96.3 (4.01)
	RTO_4t1_J13p0	209.5 (8.73)

trajectory to reach 100% coverage is reported in Table 8. All the times are well below 21 day.

Since the preliminary radar coverage analysis shows a 100% coverage for all the proposed trajectories, the scientific evaluation metric focuses on the camera scientific performances. To this end, a Camera Performance Index (CPI) has been developed to quantify the quality of observations based on angular diversity in the viewing geometry. This index measures how evenly distributed the observations of each facet of the body are across different viewing angles, with a maximum score of 1 indicating perfectly uniform coverage. Characteristics and requirements in Tables 2–4 are carefully considered, since they directly affect the allowed orbital ranges to the targets for scientific observations. One of the key requirements is achieving a specific ground sampling distance (GSD). The desired resolution is 10 cm/px, with a minimum acceptable resolution of 40 cm/px. These requirements dictate the allowable observation ranges. In addition to the GSD, phase angles also impose operational considerations. Phase angles are determined by the relative positions of the Sun, CubeSat, and asteroid. To evaluate the performance of the camera, a metric has been developed to quantify the quality of observations by assessing the angular diversity in the viewing geometry. A wide variety of viewing geometries will allow for the generation of surface radiometric models (e.g., albedo map), and increases the accuracy of shape and topography models (Palmer et al., 2022). This ensures compliance with the camera's Sun incidence requirement, another key requirement.

The metric evaluates the diversity of the viewing geometry by considering the incidence and emission angles associated with each observation of each facet. Both angular ranges are divided into five sections, as shown in Fig. 11. The resulting set of admissible angular classes is denoted by $\mathscr{B}$, while $\mathscr{F}$ denotes the set of facets of the Apophis shape model. In the present implementation, $\mathscr{B}$ contains ten angular classes, so that each newly observed class contributes 0.1 to the local score of a facet.

For each facet $f \in \mathscr{F}$ and each angular class $b \in \mathscr{B}$, the binary variable χ_{fb} is introduced as

$$\chi_{fb} = \begin{cases} 1, & \text{if facet } f \text{ is observed at least once in class } b \\ 0, & \text{otherwise} \end{cases} \tag{9}$$

Repeated observations of the same facet within the same angular class do not further increase the score. The local Camera Performance Index of facet f is then defined as

$$\mathrm{CPI}_f = \frac{1}{|\mathscr{B}|} \sum_{b \in \mathscr{B}} \chi_{fb} \tag{10}$$

and the final CPI is obtained by averaging over all facets

$$\mathrm{CPI} = \frac{1}{|\mathscr{F}|} \sum_{f \in \mathscr{F}} \mathrm{CPI}_f \tag{11}$$

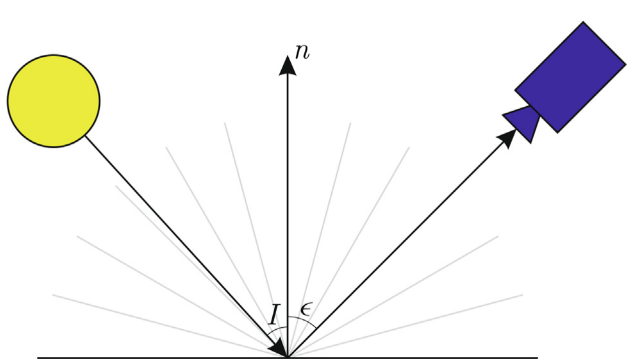

Fig. 11. Graphic visualization of the camera performance index. The angular subdivision into five sections for both incidence and emission angles is relative to the normal vector of a specific facet of the shape model.

Therefore, $\mathrm{CPI} = 1.0$ corresponds to the ideal case in which all facets are observed in all the considered angular classes.

A range-scaled index is also computed to account for the observation distance. In this case, the bin contribution $1/|\mathscr{B}|$ is replaced by the range-dependent weight

$$w = \frac{1}{|\mathscr{B}|} \min\left(\frac{R_{40\,\mathrm{cm/px}}}{r_{\min}}, 1\right) \tag{12}$$

where $R_{40\,\mathrm{cm/px}}$ is the maximum range compatible with a ground sampling distance of 40 cm/px, and $r_{\min}$ is the minimum observation range along the trajectory.

The results of this analysis for two example candidate orbits are presented in Figs. 12 and 13, showing an histogram illustrating the number of facets with a certain number of observations, the number of observations per facet, and the 2D coverage performance index for each facet. A summary of the results for all the orbits is presented, instead, in Table 9. In general, all the proposed trajectories achieve a good CPI of at least 0.7. However, the best results are obtained for RTOs with a 4:1 resonance and lower energies, as well as for 3:1 RTOs with higher energies, and for SSTO trajectories with smaller radii, which exhibit slightly higher indices. This result is further confirmed when the weighting factor is added to the index. This adjustment further lowers the index for SSTO trajectories with larger radii and for the low-CPI RTO trajectories.

Power generation RCS-1 is not equipped with a solar array driving mechanism. Hence, pointing the payloads (radar and science camera) to Apophis for scientific and navigation purposes does not always guarantee having the solar panels pointing to the Sun, which in turn reduces the power generated onboard. Thus, it is important to evaluate the power profile and its ability to keep the CubeSat running properly all the subsystems. To this end, the maximum Depth of Discharge (DoD) of the batteries is selected as evaluation metric. When this value exceeds a predefined threshold, the spacecraft enters safe mode and orients its solar panels toward the Sun to maximize power generation. If the solar panels cannot be oriented toward the Sun, the trajectory would become unfeasible. The desired attitude profile, aimed at maximizing the incoming solar power, was calculated using the following rotation matrix

$$A^*_{BN} = \begin{bmatrix} \hat{i} \\ \hat{j} \\ \hat{k} \end{bmatrix} = \begin{bmatrix} \hat{j} \times \hat{k} \\ -\frac{\hat{r} \times \hat{r}_S}{\|\hat{r} \times \hat{r}_S\|} \\ -\hat{r} \end{bmatrix} \tag{13}$$

where $\hat{r}$ is the position unit vector, and $\hat{r}$ represents the unit vector from the spacecraft center to the Sun in the spacecraft body-fixed frame. The panel-Sun angle α_P is then computed as the scalar product between the spacecraft–Sun vector in body frame and the solar panels normal (the spacecraft x-axis in this case). Fig. 14 shows the evolution of such angle throughout the 21-day simulation period, for two example candidate orbits.

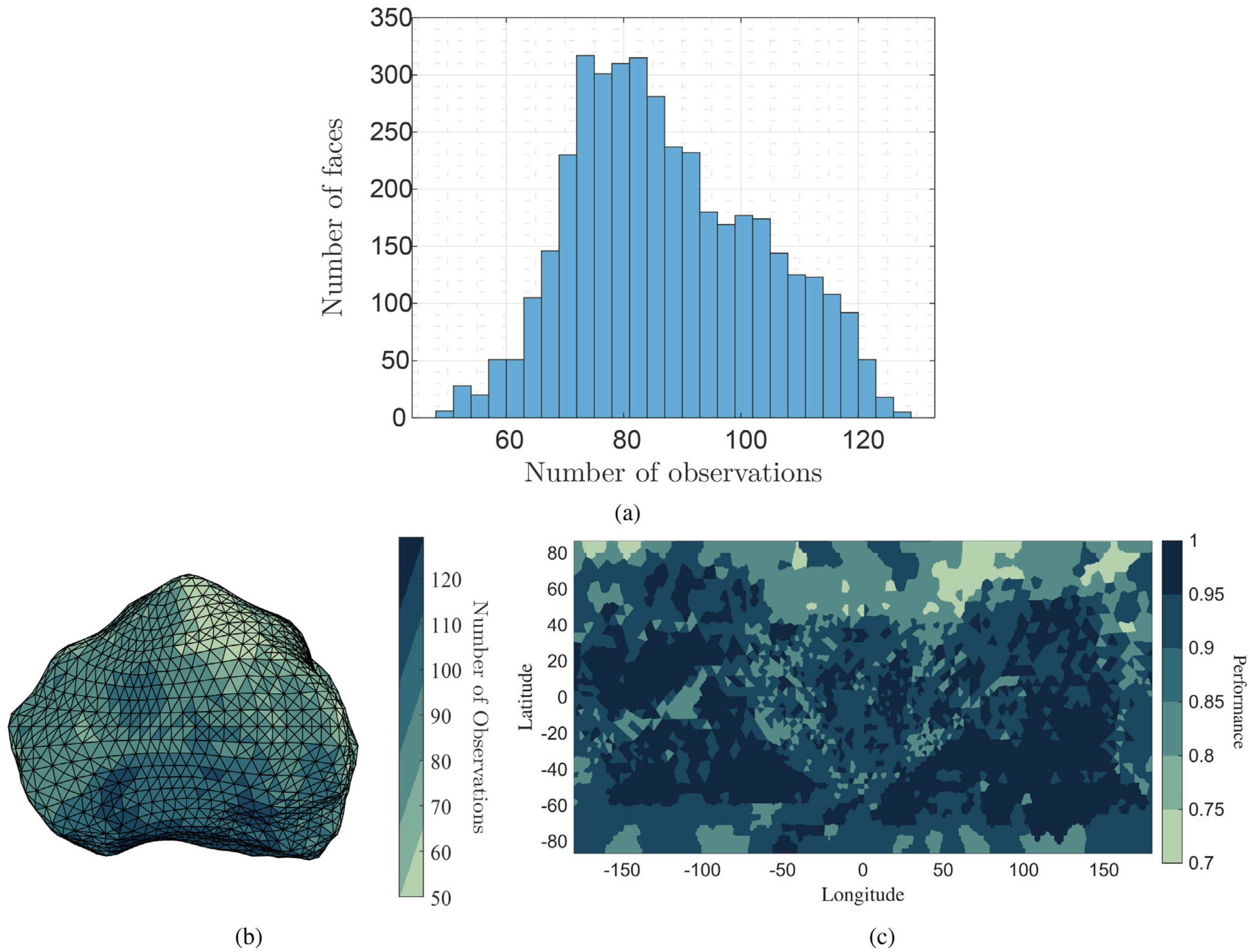

Fig. 12. Science camera analysis for SSTO_0p8: (a) Histogram of the observations for each facet; (b) shape model with colors based on the number of observations per facet; (c) 2D coverage performance index for each facet.

The spacecraft power generation has been simulated by considering the cyclic repetition of all operative modes along with their expected duty cycles. This approach allows for the simulation of both nominal and high-power demand scenarios (e.g., when the radar is active). Specifically, the power generation duty cycle is repeated over a predefined time interval, which depends on the trajectory under analysis. For SSTOs, the cycle is repeated every orbital period, defined as the average time interval between two consecutive crossings of the $x-z$ plane with a positive y-component of the spacecraft velocity. For RTOs, the cycle is repeated every petal period, which is defined as the average time interval between two consecutive minima in the spacecraft distance from the central body. While the required power depends on the spacecraft operative mode, the generated power is a function of the Panel-Sun angle α_P, the incoming solar flux P depending on the Sun distance, and the solar panels properties

$$P_{\text{in}} = \eta P \cos \alpha_P \tag{14}$$

where $\eta = 0.27$ is the efficiency. The power difference can be computed so as $\Delta P = P_{\text{in}} - P_{\text{out}}$. Once the power difference is available, the capacity of the batteries can be computed as

$$C(t) = \min\left(C_{\max}, \int_0^t \Delta P \, \mathrm{d}t + C_0\right) \tag{15}$$

where $C_{\max}$ is the maximum battery capacity and C_0, equal to 135 W h is the initial battery capacity. Finally, the DoD can be computed from the battery capacity as

$$DoD = 100\left(1 - \frac{C}{C_{\max}}\right) \tag{16}$$

Since the evaluation metric for the trajectory feasibility in terms of power is the DoD, its maximum value is used in the trade-off. The analysis indicates that none of the trajectories pose a critical risk from a power perspective. SSTOs are optimal, as they can continuously adjust their roll around the camera axis to maximize solar power intake. Consequently, power generation remains sufficient, and no critical conditions arise, with an almost constant DoD across all trajectories. Regarding RTOs, the DoD exhibits variability while never reaching critical levels, so allowing mission execution without triggering safe mode. The evolution of significant power metrics for two example candidate orbits are reported in Fig. 15.

Accumulated angular momentum Since RCS-1 shall continuously slew to have the payloads pointing to Apophis,

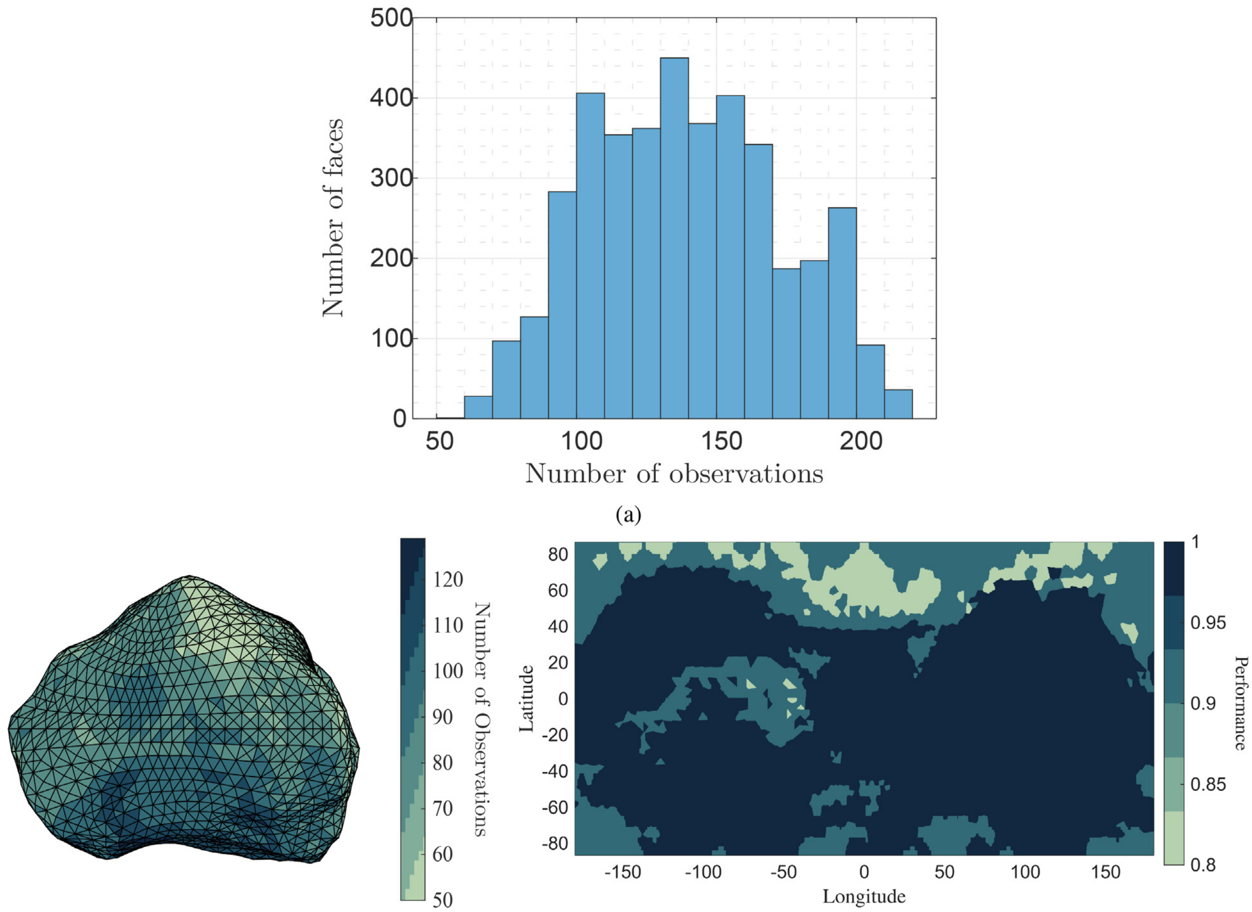

Fig. 13. Science camera analysis for RTO_4t1_J9p0: (a) Histogram of the observations for each facet; (b) shape model with colors based on the number of observations per facet; (c) 2D coverage performance index for each facet.

Table 9
Detailed trade-off summary. Colors indicate qualitative compliance classes: green for favorable cases, yellow for acceptable cases, and red for unfavorable cases.

Type	ID	Criteria				
		Scientific return	Power generation	Attitude control	Navigation accuracy	Orbit control
		CPI [-]	Max DoD [%]	h_{max} [mNms]	t_{cr} [-]	Index [-]
SSTO	SSTO_0p8	0.91742	9.94	6.03	1	1
	SSTO_1p0	0.87515	9.93	4.03	1	2
	SSTO_1p2	0.87693	9.90	2.91	1	3
	SSTO_1p4	0.85383	9.87	2.14	0.72	4
	SSTO_1p6	0.82422	9.85	1.51	0.14	3
	SSTO_1p8	0.80628	9.83	1.23	0.50	1
RTO	RTO_3t1_j13p0	0.82477	9.82	1.69	0.64	4
	RTO_3t1_j11p0	0.96614	10.88	0.16	0.31	3
	RTO_3t1_j9p0	0.97175	21.75	3.56	0.27	1
	RTO_4t1_j13p0	0.96829	9.86	0.19	0.27	3
	RTO_4t1_j11p0	0.97923	13.70	2.84	0.21	1
	RTO_4t1_j9p0	0.97685	28.50	6.53	0.18	1

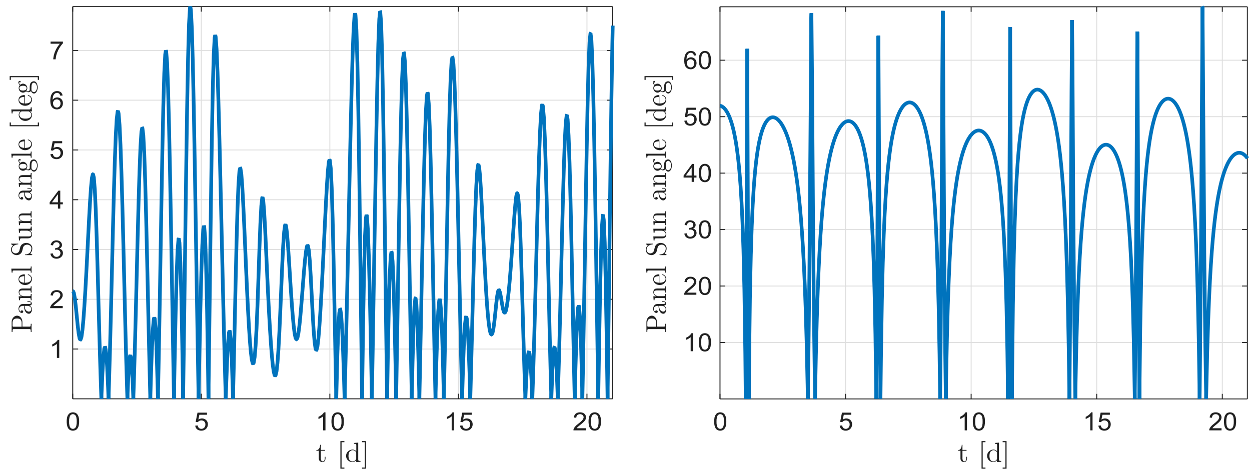

(a) (b)

Fig. 14. Time evolution for the panel Sun angle of (a) SSTO_0p8 and (b) RTO_4t1_J9p0.

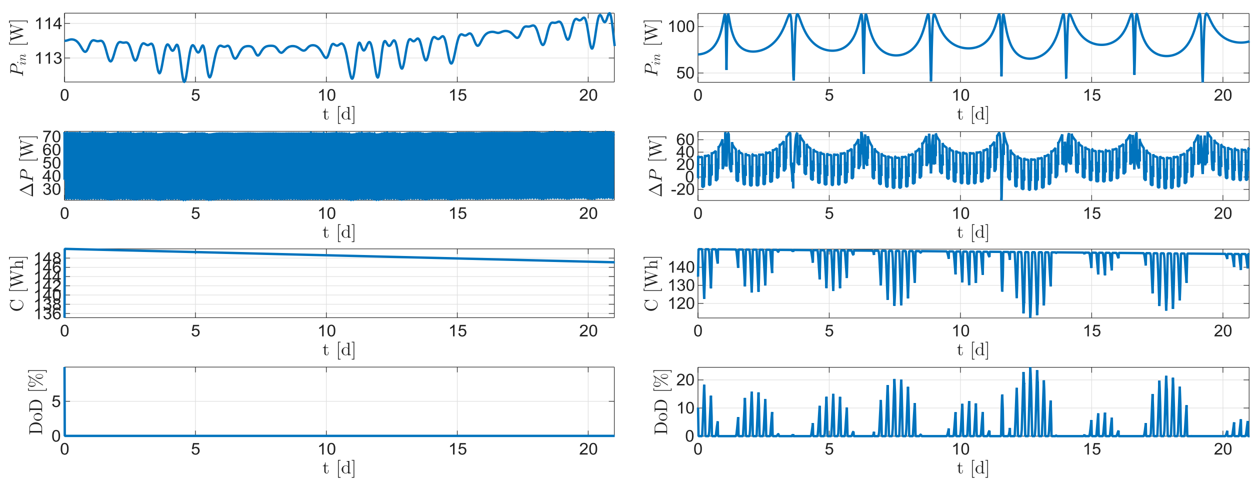

(a) (b)

Fig. 15. Time evolution for relevant power metrics of (a) SSTO_0p8 and (b) RTO_4t1_J9p0.

while maximizing the power intake, the effort required by the attitude control must be taken into account. The feasibility of the trajectories in terms of attitude control is assessed based on the maximum accumulated angular momentum on the spacecraft axes. The torque required on each spacecraft axis throughout the trajectory evolution has been computed to establish a figure of merit for attitude control. This analysis assumes the nominal attitude profile, with the spacecraft camera and radar ideally pointing toward the minor body center of mass and the solar panels continuously oriented to maximize incoming solar power. Additionally, the contribution required to counteract the torque induced by SRP has been considered, modeled through the offset between the spacecraft center of mass and center of pressure. Other perturbing torques (e.g., due to Apophis gravity field) are not explicitly included, since a preliminary order-of-magnitude assessment showed that they are approximately at least one order of magnitude smaller than the SRP-induced torque. Given the desired spacecraft attitude, the needed spacecraft angular velocity $\boldsymbol{\omega}$ and torque $\boldsymbol{\tau}$ can be computed. Specifically, given two consecutive direct cosine matrices separated by Δt, the rate of change of the direct cosine matrix can be computed as

$$\dot{A}_{BN,j} = \frac{A_{BN,j} A_{BN,j-1}^T}{\Delta t} \tag{17}$$

with A_{BN} defined as Eq. (13). Then, the angular velocity and acceleration are

$$\omega_j^{\wedge} = -\dot{A}_{BN,j} A_{BN,j}^T \tag{18}$$

$$\dot{\boldsymbol{\omega}} = \frac{\boldsymbol{\omega}_j - \boldsymbol{\omega}_{j-1}}{\Delta t} \tag{19}$$

with $\omega_j^{\wedge}$ the angular velocity skew-symmetric matrix. The torque is computed from the attitude dynamics as

$$\boldsymbol{\tau} = -J\dot{\boldsymbol{\omega}} + J\boldsymbol{\omega} \times \boldsymbol{\omega} + \boldsymbol{\tau}_p \tag{20}$$

with J the CubeSat inertia matrix and $\boldsymbol{\tau}_p$ the perturbation torque. The maximum required angular momentum throughout the trajectory, that is the figure of merit for this criterion, can be computed as

$$h_{\text{tot}} = \int_{t0}^{t_f} \boldsymbol{\tau}\, \mathrm{d}t \tag{21}$$

Two examples for the results are presented in Fig. 16.

A general summary can be found in Table 9. The maximum required torque is high for small SSTOs, where rapid trajectory evolution necessitates fast rotations to maintain pointing. This effect gradually decreases for more distant trajectories. For RTOs, the accumulated momentum has a less predictable behavior, but it increases with the energy, since more energetic orbits have a more elongated shape and so they require more pronounced rotations.

Navigation accuracy For RCS-1 the state is determined by combining visual-based navigation techniques and LIDAR altimeter measurements. The navigation metric for evaluating operative orbits is based on two key parameters: range and phase angle. The range determines whether the camera FOV is saturated, while the phase angle affects the size and the shape of the illuminated portion of the target. The figure of merit is defined as the time during which the spacecraft operates under critical conditions, which correspond to a range below $r_{\min} = 1.4$ km (i.e., when the target saturates the FOV) and a phase angle above $\varphi_{\max} = 100$ deg, as per Table 5. Formally, it is expressed as

$$t_{\text{cr}} = \frac{1}{T} \int_{t_0}^{t_f} [(r(t) < r_{\min}) \vee (\varphi(t) > \varphi_{\max})]\, \mathrm{d}t \tag{22}$$

with $T = t_f - t_0$ representing the total observation time. Lower values of t_{cr} indicate more favorable trajectories from a navigation perspective.

Orbit control Even though SSTOs and RTOs are ballistic trajectories, uncertainties due to dynamics, navigation, and maneuver execution will cause RCS-1 to deviate from its nominal trajectory. Therefore, an orbit-maintenance process is expected to be required to compensate for these deviations. At this preliminary design stage, candidate orbits are rated through a qualitative operability index. The index is based on preliminary stability checks, minimum-distance margins with respect to the asteroid, and qualitative sensitivity to TCM execution errors.

For SSTOs, higher-altitude orbits are penalized because their weaker binding to the asteroid increases the tendency toward escape under perturbations and maneuver errors. Conversely, lower-altitude SSTOs, although generally more stable, are penalized because their reduced clearance from the surface increases the consequence of TCM errors in terms of impact risk. Intermediate SSTOs therefore provide the best compromise. For RTOs, increasing the orbit energy reduces the stability margin and lowers the pericenter altitude, thereby increasing both escape and impact concerns. According to these considerations, a qualitative score from 1 to 5 is assigned to each orbit, where larger values indicate more favorable orbit-control properties.

5.3. Summary

Table 9 presents the figures of merit for all the candidates. The colors in the trade-off table indicate qualitative compliance classes: green denotes favorable or requirement-compliant cases, yellow denotes acceptable cases with reduced margin or increased operational burden, and red denotes unfavorable cases that are critical or not preferred for baseline selection. The thresholds used for the colored classification are based on the CubeSat properties, payload and navigation requirements, and operational margins discussed in Sections 3 and 5.2. SSTOs exhibit generally favourable characteristics, while low-to-medium energy RTOs demonstrate a more balanced performance across the different criteria. A closer look at Table 9 also

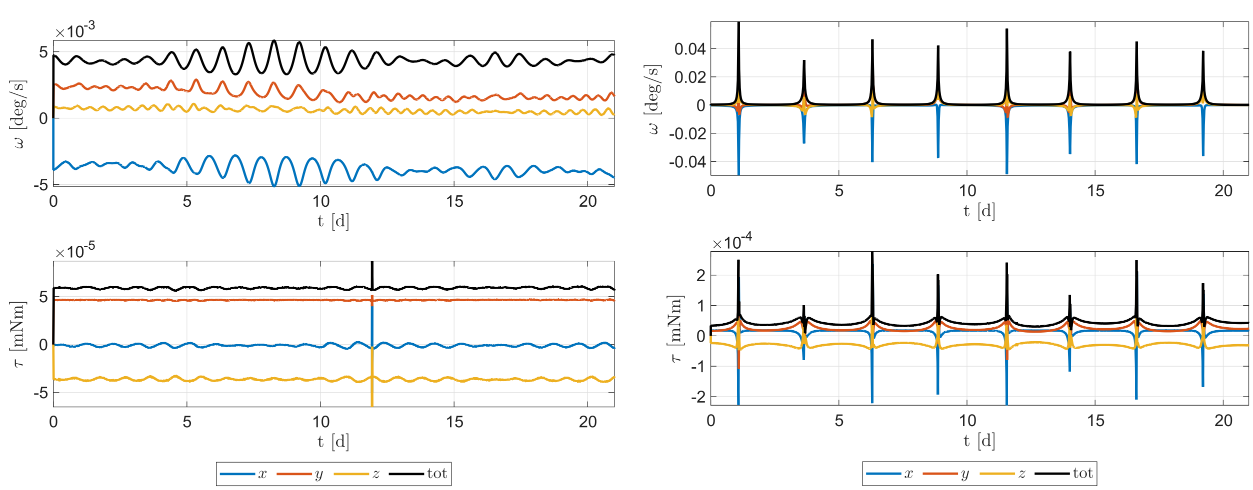

(a) (b)

Fig. 16. Time evolution for angular velocity and torque of (a) SSTO_0p8 and (b) RTO_4t1_J9p0.

highlights clear trends within each family, which are useful to interpret the trade-off beyond the aggregated statement. For SSTOs, decreasing the semimajor axis improves the CPI, as expected from the tighter ranges and more favorable observation geometry; however, it comes at the price of increased attitude-control effort and less favorable navigation conditions, since the trajectory spends a larger fraction of time either below the centroiding range threshold or at unfavorable phase angles. Conversely, larger SSTOs progressively reduce attitude-control demand and improve the navigation metric, but with a gradual degradation of CPI. This yields an intermediate sweet spot (i.e., mid-altitude SSTOs) that preserves good imaging performance while mitigating the operational penalties associated with the tightest solutions. For RTOs, the camera CPI remains consistently high across the set, confirming that resonant dynamics can naturally provide angular diversity without requiring close ranges. At the same time, increasing the orbit energy tends to penalize operability: the highest-energy cases exhibit a marked increase in battery depth of discharge and accumulated momentum, consistent with larger attitude excursions needed to reconcile payload pointing and power generation, and with more elongated petals. In this sense, low-to-medium energy RTOs emerge as the best-balanced solutions, retaining near-optimal CPI while keeping power and attitude-control requirements within comfortable margins. Therefore, the trade-off supports retaining, as primary candidates for the baseline operational orbit, either a mid-altitude SSTO (for overall simplicity and benign power behaviour) or a low-to-medium energy RTO (for the most balanced science-operability compromise). Thus, both the options could be selected as final operational orbit.

It is worth noting that orbit accessibility has not yet been considered, as no release conditions have been defined yet. However, it is anticipated that RTOs and SSTOs will have similar insertion costs, meaning accessibility is unlikely to alter the outcome. Additionally, a complete quantitative assessment for the radar has not been performed yet. It will be conducted in the next phases and would be a primary mean to close the nominal orbit trade-off. Thus, a final down selection will be provided once release conditions are defined and the radar performance is quantified with a higher-fidelity assessment.

6. Conclusions

The development of a comprehensive dynamical framework for the RAMSES's Farinella mission has enabled the identification of some optimal science orbits for the observations across the 2029 Apophis flyby. By combining a high-resolution polyhedral gravity model of Apophis with perturbations from solar radiation pressure and third-body influences, the complex acceleration environment surrounding the asteroid was accurately characterized. Three trajectory families, namely, patched hyperbolic arcs, Sun-stabilized terminator orbits, and resonant terminator orbits, were assessed against qualitative criteria, encompassing scientific return, operational simplicity, trajectory safety, and robustness. Then, specific SSTOs and RTOs are further evaluated against quantitative metrics, as imaging angular diversity, radar coverage, spacecraft power budgets, attitude control requirement. This assessment revealed that low-to-medium energy RTOs provide the most favorable balance among competing constraints, while medium-to–high SSTOs have good general characteristics. Additional investigations related to insertion costs, radar detailed output analysis, and quantitative covariance analyses, will be used in the next mission phases to close the trade-off and select a final operational orbit.

Data availability statement

Data sets generated during the current study are available from the corresponding author on request, because part of an ongoing study.

Declaration of competing interest

The authors declare that they have no known competing financial interests or personal relationships that could have appeared to influence the work reported in this paper.

Acknowledgments

Part of the work described in this paper is part of RCS-1 Phases A/B/C study, which has been funded by the European Space Agency (ESA) under ESA contract No. 4000147437/25/NL/RK. C.G. acknowledges funding from the European Union's Horizon Europe research and innovation programme under the Marie Skłodowska-Curie Grant Agreement No. 101103826. The authors would like to acknowledge Tyvak International and the whole RCS-1 Farinella Team, including ESA's experts, for their valuable support.

References

Azzola, G., 2024. A study on the mission design for Milani CubeSat to Apophis. Master's thesis. Politecnico di Milano. URL: https://hdl.handle.net/10589/231449.

Ballouz, R.L., Agrusa, H., Barnouin, O., Walsh, K., Zhang, Y., Binzel, R., Bray, V., DellaGiustina, D., Jawin, E., DeMartini, J., et al., 2024. Shaking and tumbling: short-and long-timescale mechanisms for resurfacing of near-earth asteroid surfaces from planetary tides and predictions for the 2029 Earth Encounter by (99942) Apophis. Planet. Sci. J. 5, 251. https://doi.org/10.3847/PSJ/ad84f2.

Binzel, R., Barbee, B., Barnouin, O., Bell, J., Birlan, M., Boley, A., Bottke, W., Brozovic, M., Cahill, J., Campins, H., et al., 2021. Apophis 2029: decadal opportunity for the science of planetary defense. Bull. AAS 53. https://doi.org/10.3847/25c2cfeb.f87e0599.

Bottiglieri, C., Piccolo, F., Giordano, C., Ferrari, F., Topputo, F., 2023. Applied trajectory design for CubeSat close-proximity operations around asteroids: the Milani case. Aerospace 10, 464. https://doi.org/10.3390/aerospace10050464.

Broschart, S.B., Lantoine, G., Grebow, D.J., 2014. Quasi-terminator orbits near primitive bodies. Celest. Mech. Dynam. Astron. 120, 195–215. https://doi.org/10.1007/s10569-014-9574-3.

Brozović, M., Benner, L.A., McMichael, J.G., Giorgini, J.D., Pravec, P., Scheirich, P., Magri, C., Busch, M.W., Jao, J.S., Lee, C.G., et al., 2018. Goldstone and Arecibo radar observations of (99942) Apophis in 2012–2013. Icarus 300, 115–128. https://doi.org/10.1016/j.icarus.2017.08.032.

Buonagura, C., Pugliatti, M., Topputo, F., 2024. MONET: the minor body generator tool at DART Lab. Sensors 24, 3658. https://doi.org/10.3390/s24113658.

Burattini, C., Colombo, C., Trisolini, M., 2024. Aerogel-based collection of ejecta material from asteroids from libration point orbits: dynamics and capture design. Astrodynamics 8, 529–551. https://doi.org/10.1007/s42064-023-0197-x.

Chesley, S.R., 2005. Potential impact detection for near-Earth asteroids: the case of 99942 Apophis (2004 MN4). Proc. Int. Astron. Union 1, 215–228. https://doi.org/10.1017/S1743921305006769.

DellaGiustina, D., Golish, D., Guzewich, S., Moreau, M., Nolan, M., Polit, A., Simon, A., 2022. Osiris-APEX: a proposed OSIRIS-REx extended mission to Apophis. LPI Contribut. 2681, 2011.

DeMartini, J.V., Richardson, D.C., Barnouin, O.S., Schmerr, N.C., Plescia, J.B., Scheirich, P., Pravec, P., 2019. Using a discrete element method to investigate seismic response and spin change of 99942 Apophis during its 2029 tidal encounter with Earth. Icarus 328, 93–103. https://doi.org/10.1016/j.icarus.2019.03.015.

Ferrari, F., Franzese, V., Pugliatti, M., Giordano, C., Topputo, F., 2021. Preliminary mission profile of Hera's Milani CubeSat. Adv. Space Res. 67, 2010–2029. https://doi.org/10.1016/j.asr.2020.12.034.

Ferrari, F., Franzese, V., Pugliatti, M., Giordano, C., Topputo, F., 2021. Trajectory options for Hera's Milani CubeSat around (65803) Didymos. J. Astronaut. Sci. 68, 973–994. https://doi.org/10.1007/s40295-021-00282-z.

Giorgini, J.D., Benner, L.A., Ostro, S.J., Nolan, M.C., Busch, M.W., 2008. Predicting the Earth encounters of (99942) Apophis. Icarus 193, 1–19. https://doi.org/10.1016/j.icarus.2007.09.012.

Goldberg, H.R., Karatekin, Ö., Ritter, B., Herique, A., Tortora, P., Prioroc, C., Gutierrez, B.G., Martino, P., Carnelli, I., 2019. The Juventas CubeSat in Support of ESA's Hera Mission to the Asteroid Didymos, in: Small Satellite Conference, Logan, UT. doi:10.15142/h8t3-3s29. sSC19-WKIV-05.

Haynes, M.S., Fenni, I., Gim, Y., Kofman, W., Herique, A., 2021. Angular and radial sampling criteria for monostatic and bistatic radar tomography of solar system small bodies. Adv. Space Res. 68, 3903–3924. https://doi.org/10.1016/j.asr.2021.07.035.

Kim, Y., DeMartini, J.V., Richardson, D.C., Hirabayashi, M., 2023. Tidal resurfacing model for (99942) Apophis during the 2029 close approach with Earth. Mon. Not. R. Astron. Soc. 520, 3405–3415. https://doi.org/10.1093/mnras/stad351.

Kueppers, M., Martino, P., Carnelli, I., Michel, P., 2023. Ramses–ESA's study for a small mission to apophis. AAS/Divis. Planet. Sci. Meet. Abstr.# 55, 201–208.

Li, X., Scheeres, D.J., 2021. The shape and surface environment of 2016 HO3. Icarus 357, 114249. https://doi.org/10.1016/j.icarus.2020.114249.

Li, X., Scheeres, D.J., Qiao, D., Liu, Z., 2023. Geophysical and orbital environments of asteroid 469219 2016 HO3. Astrodynamics 7, 31–50. https://doi.org/10.1007/s42064-022-0131-7.

McMahon, J., Scheeres, D., Hesar, S., Farnocchia, D., Chesley, S., Lauretta, D., 2018. The OSIRIS-REx radio science experiment at Bennu. Space Sci. Rev. 214, 1–41. https://doi.org/10.1007/s11214-018-0480-y.

Morelli, A.C., Mannocchi, A., Giordano, C., Ferrari, F., Topputo, F., 2024. Initial trajectory assessment of a low-thrust option for the RAMSES Mission to (99942) Apophis. Adv. Space Res. 73, 4241–4253. https://doi.org/10.1016/j.asr.2024.02.005.

Palmer, E.E., Gaskell, R., Daly, M.G., Barnouin, O.S., Adam, C.D., Lauretta, D.S., 2022. Practical stereophotoclinometry for modeling shape and topography on planetary missions. Planet. Sci. J. 3, 102. https://doi.org/10.3847/PSJ/ac460f.

Pérez-Ayúcar, M., Ashman, M., Almeida, M., Sitja, M.C., Beteta, J.J.G., Hoofs, R., Kueppers, M., Yaseli, J.M., Merritt, D., Nespoli, F., et al., 2018. The Rosetta science operations and planning implementation. Acta Astronaut. 152, 163–174. https://doi.org/10.1016/j.actaastro.2018.07.049.

Pravec, P., Scheirich, P., Ďurech, J., Pollock, J., Kušnirák, P., Hornoch, K., Galád, A., Vokrouhlicky', D., Harris, A., Jehin, E., et al., 2014. The tumbling spin state of (99942) Apophis. Icarus 233, 48–60. https://doi.org/10.1016/j.icarus.2014.01.026.

Pugliatti, M., Buonagura, C., Topputo, F., 2023. CORTO: the celestial object rendering TOol at DART Lab. Sensors 23, 9595. https://doi.org/10.3390/s23239595.

Scheeres, D., 2012. Orbital mechanics about small bodies. Acta Astronaut. 72, 1–14. https://doi.org/10.1016/j.actaastro.2011.10.021.

Scheeres, D., Benner, L., Ostro, S., Rossi, A., Marzari, F., Washabaugh, P., 2005. Abrupt alteration of Asteroid 2004 MN4's spin state during its 2029 Earth flyby. Icarus 178, 281–283. https://doi.org/10.1016/j.icarus.2005.06.002.

Sokolov, L., Bashakov, A., Borisova, T., Petrov, N., Pitjev, N., Shaidulin, V.S., 2012. Impact trajectories of the asteroid Apophis in the 21st century. Sol. Syst. Res. 46, 291–300. https://doi.org/10.1134/S0038094612040077.

Souchay, J., Souami, D., Lhotka, C., Puente, V., Folgueira, M., 2014. Rotational changes of the asteroid 99942 Apophis during the 2029 close encounter with Earth. Astron. Astrophys. 563, A24. https://doi.org/10.1051/0004-6361/201322364.

Takahashi, S., Scheeres, D.J., 2020. Higher-order corrections for frozen terminator orbit design. J. Guid., Control, Dynam. 43, 1642–1655. https://doi.org/10.2514/1.G004901.

Valvano, G., Winter, O.C., Sfair, R., Machado Oliveira, R., Borderes-Motta, G., Moura, T., 2022. Apophis – effects of the 2029 Earth's encounter on the surface and nearby dynamics. Mon. Not. R. Astron. Soc. 510, 95–109. https://doi.org/10.1093/mnras/stab3299.

Wen, T., Zeng, X., 2023. Equilibrium points of heterogeneous small body in finite element method. Mon. Not. R. Astron. Soc. 519, 6077–6087. https://doi.org/10.1093/mnras/stad119.

Werner, R.A., 1994. The gravitational potential of a homogeneous polyhedron or don't cut corners. Celest. Mech. Dynam. Astron. 59, 253–278. https://doi.org/10.1007/BF00692875.

Werner, R.A., Scheeres, D.J., 1996. Exterior gravitation of a polyhedron derived and compared with harmonic and mascon gravitation representations of asteroid 4769 Castalia. Celest. Mech. Dynam. Astron. 65, 313–344. https://doi.org/10.1007/BF00053511.

Yu, Y., Richardson, D.C., Michel, P., Schwartz, S.R., Ballouz, R.L., 2014. Numerical predictions of surface effects during the 2029 close approach of asteroid 99942 Apophis. Icarus 242, 82–96. https://doi.org/10.1016/j.icarus.2014.07.027.

Zhang, Y., Michel, P., 2020. Tidal distortion and disruption of rubble-pile bodies revisited-soft-sphere discrete element analyses. Astron. Astrophys. 640, A102. https://doi.org/10.1051/0004-6361/202037856.